JCTC Journal of Chemical Theory and Computation

Photoisomerization of Model Retinal Chromophores: Insight from Quantum Monte Carlo and Multiconfigurational Perturbation Theory

Omar Valsson* and Claudia Filippi*

Faculty of Science and Technology and MESA+ Research Institute, University of Twente, P.O. Box 217, 7500 AE Enschede, The Netherlands

Received December 26, 2009

Abstract: We present a systematic investigation of the structural relaxation in the excited state of model retinal chromophores in the gas phase using the complete-active-space self-consistent theory (CASSCF), multiconfigurational second-order perturbation theory (CASPT2), quantum Monte Carlo (QMC), and coupled cluster (CC) methods. In contrast to the CASSCF photoisomerization mechanism of bond inversion followed by torsion around formal double bonds, we find that the other approaches predict an initial skeletal relaxation which does not lead to bond inversion but to a rather flexible retinal chromophore with longer bonds and with the bond-length pattern of the ground state being partly preserved. The relaxation proceeds then preferentially via partial torsion around formal single bonds and does not reach a conical intersection region. Our findings are compatible with solution experiments which point to the existence of multiple minima and relaxation pathways, some of which are nonreactive, do not lead to photoproducts via conical intersection, and are dominant in solution. Our results also demonstrate the importance of a balanced description of dynamical and static correlation in the excited-state gradients and raise serious concerns on the common use of the CASSCF method to investigate structural properties of photoexcited retinal systems.

1. Introduction

The absorption of visible light and its conversion to other forms of energy is at the heart of some of the most fundamental processes in biology. An important example of light absorption initiating a biological response is the primary event of vision[1] where light induces the *cis*−*trans* isomerization of the photosensitive 11-*cis* retinal chromophore in rhodopsin[2] and other visual pigments, activating a cascade of chemical reactions which ultimately culminate in the stimulation of the optical nerve.[3] The initial photoisomerization process is one of the fastest photochemical reactions in nature, occurring within a few hundred femtoseconds,[4] and the protein environment plays a central role in guiding the reaction. In solution, the dynamics of retinal chromophores is in fact quite different than in the protein, namely, about 20 times slower[5] and much less efficient.[6,7] Even though femtosecond spectroscopy studies have extensively investigated the primary isomerization step of retinal chromophores,[8−14] the detailed nature of the molecular mechanism in the initial excited-state reaction and the exact role of the protein environment are still not understood.[12]

Theoretically, a large number of calculations with a variety of quantum chemical methods have been performed to investigate the structural and spectroscopic properties as well as the nature of the photoisomerization mechanism of retinal chromophores and retinal models in the gas phase[15−41] and in the protein environment.[24,42−61] Given the large size of the retinal chromophore, most calculations including the protein via quantum mechanics/molecular mechanics (QM/MM) approaches have mainly focused on obtaining a realistic representation of the structural model in the ground state and understanding the environmental effects on the absorption properties. Interestingly, even though all investigations employing different techniques appear to reproduce the correct experimental absorption value, the reasons behind

* Authors' e-mail: o.valsson@utwente.nl (O.V.); c.filippi@utwente.nl (C.F.).

10.1021/ct900692y
Published on Web 03/12/2010

this agreement are contrasting and there are fundamental differences concerning the structure of the chromophore, the protonation of nearby residues, and the overall role of the protein in tuning the spectral properties.[46,52,53,57,60] If nailing down the exact role of the environment on the Franck−Condon excitation has proven elusive, the computation of dynamical properties of photoexcited retinal chromophores in the gas phase as well as in the protein is an even harder task since it requires a uniformly reliable computation of excited-state potential energy surfaces and the availability of analytical energy gradients for geometric optimization and dynamical runs.

To date, most excited-state geometrical investigations have employed the low-level complete-active-space self-consistent field (CASSCF) approach for the relaxation of retinal chromophores in the gas phase[15−18,33,34,38,46] with also few attempts to simulate the dynamics of retinal chromophores in the protein environment.[45,55,61] The excited-state energies on the CASSCF structures are often refined in single-point calculations with higher-level approaches such as multiconfigurational perturbation theory (CASPT2) to partially account for dynamical correlation largely missing in the CASSCF description. These studies have led to the generally accepted picture that photoisomerization begins with an in-plane skeletal relaxation which yields bond inversion and proceeds via a torsional motion around carbon−carbon bonds having double-bond character in the ground state.[16,18,34,38] The chromophore is then funneled into a conical intersection region which leads to the ground-state *trans* photoproduct. Recent calculations of Send and Sundholm based on coupled cluster (CC) theory have however challenged this picture, as they obtained a rather different excited-state relaxation mechanism of retinal models in the gas phase.[29,31,35,37] The initial relaxation in the excited state at the CC level does not yield bond inversion but the lengthening of most bonds while preserving the general bond-length pattern of the ground state. The subsequent torsional motion is around carbon−carbon bonds holding single-bond character in the ground state. However, these CC calculations have been dismissed on the basis of being single reference and thus lacking a proper description of static correlation as compared to the CASSCF approach.[36] This response reflects the general acceptance of CASSCF as an adequate tool for the investigation of excited-state structural properties of retinal and other photosensitive chromophores.

In the present work, we perform a thorough investigation of the initial excited-state relaxation from the Franck−Condon point of model retinal chromophores in the gas phase and employ CASPT2 and quantum Monte Carlo (QMC) in addition to the CASSCF and CC methods. The CASPT2 approach is well established and is considered a benchmark method for the computation of excited-state properties, but its use for retinal models has been mostly confined to single-point calculations, in-plane geometrical relaxation of few models,[20] and constraint optimization of a minimal chromophore model.[19,20,23,41] The QMC method is instead less common in the field of theoretical photochemistry, and its use for excited-state geometrical optimization is novel. QMC has recently given promising results in the study of various photoactive molecules,[62−66] and a favorable comparison with CASPT2 will further establish its use for investigating photochemical problems. At the cost of being computationally more expensive, CASPT2 and QMC methods can give an accurate and balanced description of both static and dynamical correlation and therefore represent an ideal tool to clarify the nature of the microscopic mechanism in the photoisomerization of retinal chromophores and to resolve the disagreement between the generally accepted CASSCF picture and the recent, controversial CC results.

We find that our in-plane geometrical relaxations from the Franck−Condon point of retinal models show a consistent, good agreement among the CASPT2, CC, and QMC approaches, which give excited-state structures not characterized by bond-length inversion, and are in striking contrast to the results obtained with the CASSCF approach. Photoexcitation therefore weakens all bonds, which stretch and become partly more similar in length while preserving the general bond-length pattern of the ground state. To investigate a nontrivial minimum energy path out of plane, we consider a model with four double bonds and find that the excited-state relaxation at the CASPT2 level proceeds preferentially via a partial torsional motion around a formal single bond and does not lead to a conical intersection region. To assess the existence of a reactive path at the CASPT2 level, we also study the constrained excited-state isomerization around a formal double bond for the same model. We find that the system encounters a small barrier to isomerization at rather large angles of rotation, beyond which it is funneled toward a conical intersection region characterized by bond inversion.

Therefore, in agreement with previous CC calculations, our results support the picture of a rather flexible retinal chromophore in the excited state as compared to the CASSCF excited chromophore, which can only twist around formal double bonds. These findings are compatible with the observation in solution experiments of the existence of multiple minima, possibly corresponding to different torsional conformations, and multiple excited-state paths. Some of these paths are reactive and yield a photoproduct via a conical intersection, while others are nonreactive, do not lead to a conical intersection, and are dominant in solution.[67] Finally, our results demonstrate the importance of including an accurate description of dynamical correlation also in the excited-state gradients and raise serious concerns about the common use of CASSCF in investigating excited-state structures of retinal systems.

In section 2, we briefly present the methods used in this paper and focus on the description of the QMC geometrical optimization. In section 3, we describe the computational details, and in section 4, we introduce the model retinal chromophores we investigate. In sections 5−7, we present the results for the vertical excitation energy, the in-plane geometrical relaxation, and the minimum energy path or out-of-plane geometrical relaxation in the excited state. Finally, in section 8, we discuss our results and conclude.

2. Methods

In this work, we employ a wide range of ab initio quantum chemical methods. While we refer the reader to appropriate

textbooks[68] for a discussion of the more traditional CASSCF, CASPT2, and CC approaches, we briefly review below the less common QMC methods.[69] In particular, we focus on the procedure we follow to perform geometrical optimization within variational Monte Carlo (VMC), which is nonstandard, and on how we address stability issues in the calculation of energy gradients.

2.1. QMC Methods. QMC methods provide an accurate and balanced description of dynamical and static electronic correlation in both molecular and extended systems.[69] Their application to the description of the excited-state properties of photoactive molecules has already given promising results.[62−66]

A crucial ingredient which determines the quality of a QMC calculation is the many-body trial wave function, which is here chosen to be of the so-called Jastrow-Slater type. Since we treat multiple states of the same symmetry, we write the ground- and excited-state wave functions as a linear combination of spin-adapted configuration state functions (CSF) multiplied by a Jastrow correlation factor:

$$\psi_I = \mathscr{J}\sum_{i=1}^{N_{\mathrm{CSF}}} c_i^I C_i \tag{1}$$

where different states depend on their individual linear coefficients, c_i^I, but share a common set of single-particle orbitals and Jastrow factor, $\mathscr{J}$. We use here a Jastrow factor which correlates pairs of electrons and each electron separately with a nucleus, and we employ different Jastrow factors to describe the correlation with different atom types. Since the optimal orbitals and expansion coefficients in ψ_I may differ from the values obtained for instance in a CASSCF calculation in the absence of the Jastrow factor, it is important to reoptimize them in the presence of the Jastrow factor.

The parameters of the trial wave functions are optimized in an efficient and simple approach in a state-average (SA) fashion as described in ref 66. In this scheme, we iteratively alternate between optimizing the linear coefficients in the CSF expansion and the nonlinear (Jastrow and orbital) coefficients where the quantity minimized is the weighted averaged energy over the states under consideration:

$$E_{\mathrm{SA}} = \sum_I w_I \frac{\langle \Psi_I | \mathscr{H} | \Psi_I \rangle}{\langle \Psi_I | \Psi_I \rangle} \tag{2}$$

where the weights are fixed and $\sum_I w_I = 1$. At convergence, the averaged energy E_{SA} is stationary with respect to all parameter variations subject to the orthogonality constraint, while the energies of the states are stationary with respect to variations of the linear coefficients but not of the orbital or Jastrow parameters. In this approach, the wave functions are kept orthogonal and a generalized variational theorem applies.

The set of optimal linear coefficients is obtained by solving a generalized eigenvalue problem where the Hamiltonian and the overlap matrix on the basis functions $\mathscr{J}C_i$ are estimated within VMC by sampling a guiding function Ψ_g chosen to have significant overlap with all states of interest. The use of a nonsymmetric estimator of the Hamiltonian matrix yields a strong zero-variance principle and renders the approach particularly efficient.[70] To optimize the nonlinear parameters, we employ the linear optimization method first developed for ground states[71] and recently extended to the state-average optimization of multiple states.[66] In this scheme, the nonlinear minimization problem is linearized by working on the basis of the derivatives of the wave function with respect to the nonlinear parameters. In the case of multiple states, the elements of the weighted averaged Hamiltonian and overlap matrices are computed in a single VMC run by sampling a guiding wave function Ψ_g. When determining both the linear and the nonlinear parameters, the guiding wave function is here chosen equal to $\sqrt{(\Sigma_I |\Psi_I|^2)}$.

The optimal trial wave functions are then used in diffusion Monte Carlo (DMC), which gives the best energy within the fixed-node approximation, that is, the lowest-energy state with the same zeros (nodes) as the trial wave function.

2.2. VMC Geometrical Optimization. The VMC geometrical optimization is performed in Z-matrix coordinates where the energy gradients with respect to the nuclear coordinates are obtained using numerical differentiation and correlated sampling.[72]

To determine the interatomic forces at a given reference geometry, we construct a set of secondary geometries corresponding to small forward and backward displacements of 0.001 au for the bond lengths and 0.01° for the bond and dihedral angles. The gradient in Z-matrix coordinates is computed as

$$\mathbf{g}_\gamma = [E(\mathbf{x} + \delta x_\gamma) - E(\mathbf{x} - \delta x_\gamma)]/2\delta x_\gamma \tag{3}$$

where E is the total energy and δx_γ is a displacement in the internal coordinate γ with respect to the reference coordinates $\mathbf{x}$. The diagonal component of the Hessian can be obtained in the same run at no extra cost as

$$\mathbf{h}_\gamma^{\mathrm{diag}} = [E(\mathbf{x} + \delta x_\gamma) - 2E(\mathbf{x}) + E(\mathbf{x} - \delta x_\gamma)]/\delta x_\gamma^2 \tag{4}$$

The geometry is updated according to an approximate version of the Newton−Raphson method as

$$\mathbf{x}'_\gamma = \mathbf{x}_\gamma - \mathbf{g}_\gamma/\mathbf{h}_\gamma^{\mathrm{diag}} \tag{5}$$

where $\mathbf{x}'$ denotes the new coordinates in Z-matrix representation. To stabilize the procedure against numerical noise, we add a constant parameter of 5×10^{-5} to all diagonal elements of the Hessian.

The use of correlated sampling allows us to efficiently determine relative energies for different geometries from a single reference Monte Carlo walk. The reference walk is obtained by sampling the wave function Ψ corresponding to the coordinates $\mathbf{x}$ and Hamiltonian $\mathscr{H}$, while the secondary geometries are characterized by the corresponding quantities $\mathbf{x} \pm \delta x_\gamma$, Ψ_γ, and $\mathscr{H}_\gamma$. Given a reference primary wave function, the secondary wave function is here simply obtained by recentering Ψ at the coordinates $\mathbf{x} \pm \delta x_\gamma$ without altering the wave function parameters. The electronic coordinates of the secondary walk are obtained by stretching the primary walk with the nuclear coordinates through a space-warp transformation as described in ref 72. In the present work, we use the function $F(r) = r^{-4}$ for the space-warp transformation.

In summary, the procedure for the geometrical optimization is the following: (*i*) The determinantal component of the initial wave function is obtained in a CASSCF calculation. (*ii*) All wave function parameters are optimized in a VMC run (we discuss later the importance of optimizing the orbital parameters). (*iii*) The energy gradients are obtained in a correlated sampling VMC calculation. (*iv*) The geometry is updated as described above. We note that, with the exception of the first iteration, step *i* can be skipped since step *ii* can be performed starting from the wave function optimized at the previous geometry and recentered at the current geometry. This procedure is iterated until the bond length and bond angle gradients are on the order of 0.001 hartree/Bohr and 0.0001 hartree/deg, respectively, that is, comparable to their error bars. Since the stochastic nature of VMC does not allow the assignment of one particular geometry as the minimum one, we perform 5−10 additional iterations after convergence and average the internal coordinates over these additional steps.

To decrease the computational effort, the carbon−hydrogen and nitrogen−hydrogen bond lengths and all the bond angles involving terminal hydrogen atoms are kept fixed. All other internal degrees of freedom are allowed to vary.

2.3. Stability of VMC Energy Gradients. The computation of gradients in VMC poses some stability issues which we analyze by considering for simplicity the gradient expression without the use of the space-warp transformation. Then, the energy difference between the primary and a secondary geometry can be written as

$$E(\mathbf{x}) - E(\mathbf{x} + \delta x_\gamma) = \left\langle \frac{\mathscr{H}\Psi(\mathbf{R})}{\Psi(\mathbf{R})} - \frac{\mathscr{H}_\gamma \Psi_\gamma(\mathbf{R})}{\Psi_\gamma(\mathbf{R})} W_\gamma(\mathbf{R}) \right\rangle_{\Psi^2} \tag{6}$$

where $\langle \cdots \rangle$ denotes the statistical average over the configurations sampled in VMC from the distribution Ψ^2, and the weights are defined as

$$W_\gamma(\mathbf{R}) = \frac{\Psi_\gamma^2(\mathbf{R})/\Psi^2(\mathbf{R})}{\langle \Psi_\gamma^2(\mathbf{R})/\Psi^2(\mathbf{R}) \rangle_{\Psi^2}} \tag{7}$$

If we expand this energy difference to linear order in δx_γ, we obtain a term proportional to

$$\left\langle \frac{\mathscr{H}\Psi(\mathbf{R})}{\Psi(\mathbf{R})} \frac{\partial \log \Psi(\mathbf{R})}{\partial x_\gamma} \right\rangle_{\Psi^2} \tag{8}$$

Since the product inside the square brackets diverges as $1/d^2$ when the distance d from the nodes of Ψ approaches zero, the estimator of eq 6 obtained by sampling the square of the primary wave function has infinite variance, and it is not possible to obtain a stable energy difference. To cure this problem, we follow ref 73 and sample a different distribution which is nonzero at the nodes and is defined here as

$$\Psi_g(\mathbf{R}) = \Psi(\mathbf{R}) \frac{\max[\varepsilon, d_n(\mathbf{R})]}{d_n(\mathbf{R})} \tag{9}$$

where $d_n(\mathbf{R})$ is a measure of the distance from the nodes:

$$d_n(\mathbf{R}) = \frac{1}{|\nabla \Psi(\mathbf{R})/\Psi(\mathbf{R})|} \tag{10}$$

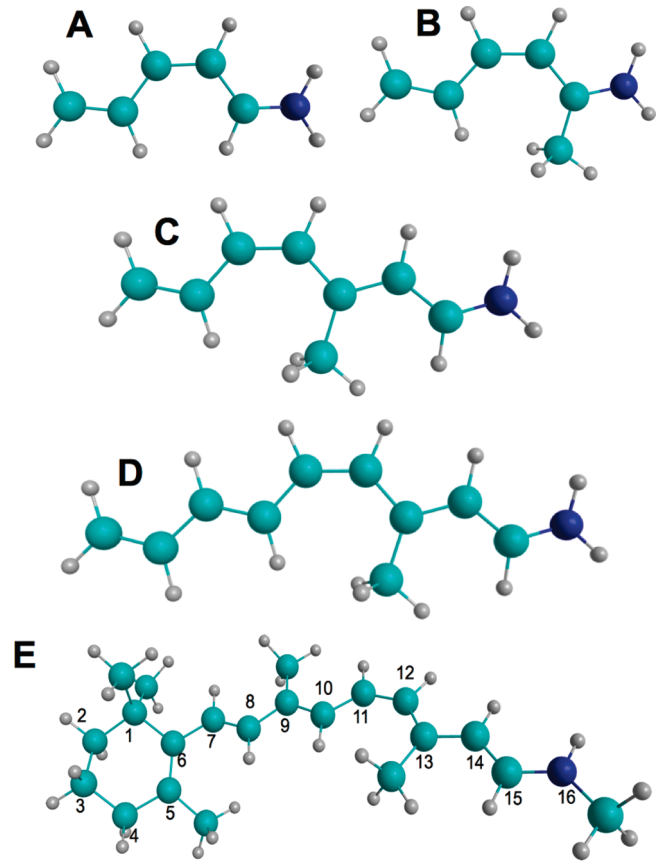

Figure 1. Model retinal chromophores. The atom numbering for chromophore E is used for all models, so the *cis* bond is always between C_{11} and C_{12}. Cyan, blue, and gray represent carbon, nitrogen, and hydrogen, respectively.

and ε is a cutoff parameter[74] chosen as 10^{-2}. The average of eq 8 can then be rewritten as

$$\left\langle \frac{\Psi^2(\mathbf{R})}{\Psi_g^2(\mathbf{R})} \frac{\mathscr{H}\Psi(\mathbf{R})}{\Psi(\mathbf{R})} \frac{\partial \log \Psi(\mathbf{R})}{\partial x_\gamma} \right\rangle_{\Psi_g^2} \tag{11}$$

where the reweighting factor $\Psi^2(\mathbf{R})/\Psi_g^2(\mathbf{R})$ removes the divergence of the products inside the brackets. This cures the problem of the infinite variance and allows us to obtain stable energy differences.

3. Computational Details

We use the program MOLCAS 7.2[75] to optimize the ground-state geometries of the model chromophores within all-electron MP2 and DFT with the B3LYP[76] functional. For the ground-state optimizations of the full retinal model (see Figure 1E), we employ the Gaussian 03 code.[77] The default convergence criteria are used for both codes.

We also use MOLCAS 7.2 for the all-electron CASSCF, CASPT2, and multistate (MS) CASPT2[78] calculations. The state-average (SA) CASSCF calculations are performed with equal weights over the states of interest, and the two lowest states are used in the SA-CASSCF and MS-CASPT2 calculations. In the CASPT2 calculations, we employ the default IPEA zero-order Hamiltonian[79] unless otherwise stated and indicate if an additional constant level shift[80] is added to the Hamiltonian. In the CASPT2 calculations for

the complete 11-*cis* retinal chromophore, we use the Cholesky decomposition of the two-electron integrals[81] with a default threshold of 10^{-4}. Analytical CASSCF and numerical CASPT2 gradients are used for geometrical optimizations and minimum energy path (MEP) calculations. In the CASPT2 calculations, we do not correlate as many lowest orbitals of σ character as the number of heavy atoms in the model. The default convergence criteria are used for all calculations.

The EOM-CC calculations are performed with the codes ACES II[82] and CFOUR.[83] The CC calculations include approximate single and double excitations (CC2) and single and double excitations (CCSD). Default convergence criteria are used for all calculations, and we do not correlate as many lowest orbitals of σ character as the number of heavy atoms in the model.

The program package CHAMP[84] is used for the QMC calculations. We employ scalar-relativistic energy-consistent Hartree−Fock pseudopotentials[85] where the carbon, nitrogen, and oxygen 1s electrons are replaced by a nonsingular s-nonlocal pseudopotential and the hydrogen potential is softened by removing the Coulomb divergence. Different Jastrow factors are used to describe the correlation with different atom types, and for each atom type, the Jastrow factor consists of an exponential of the sum of two fifth-order polynomials of the electron−nuclear and the electron−electron distances, respectively.[86] We also test the effect of including an electron−electron−nuclear term. The starting determinantal components are obtained in CASSCF calculations, which are performed with the program GAMESS(US).[87] In all SA-CASSCF calculations, equal weights over the states are employed and the final CAS expansions are expressed on the weighted-average CASSCF natural orbitals. The CAS wave functions of the ground and excited states may be truncated with an appropriate threshold on the CSF coefficients, and the union sets of surviving CSFs for the states of interest are retained in the QMC calculations. The Jastrow correlation factor and the CI coefficients are optimized by energy minimization in a state-averaged sense within VMC with equal weights. When indicated in the text, also the orbitals are optimized along with the Jastrow and CI parameters. The pseudopotentials are treated beyond the locality approximation,[88] and an imaginary time step of 0.05 or 0.075 au is used in the DMC calculations.

In the DFT, CASSCF, CASPT2, and CC calculations, we employ either the correlation consistent (cc-pVxZ)[89] or the atomic natural orbital (ANO-L-VxZP)[90] basis sets. We use the ANO contraction schemes as defined in MOLCAS, that is, [3s2p1d]/[2s1p] for ANO-L-VDZP, [4s3p2d1f]/[3s2p1d] for ANO-L-VTZP, and [5s4p3d2f]/[4s3p2d] for ANO-L-VQZP. In the single-point energy calculations, the ANO-L-VDZP basis set is generally used, while the default basis in the geometrical optimization and MEP calculations is the cc-pVDZ. In the QMC calculations, we use the Gaussian basis sets[85] specifically constructed for our pseudopotentials. In particular, we employ the cc-pVDZ basis (denoted by D) and the D basis augmented with s and p diffuse functions[91] on the heavy atoms (denoted by D+). We also use the T′ and Q′ basis sets which consist of the cc-pVTZ and cc-pVQZ, respectively, combined with the cc-pVDZ for hydrogen. The g functions are not included in the Q′ basis. Most single-point energy calculations use the D+ basis, while geometrical optimizations employ the D basis.

4. Retinal Models

The 11-*cis* retinal chromophore consists of a conjugated carbon chain with a protonated Schiff base (PSB) at one end and a twisted β-ionone ring at the other end (see Figure 1E). It sits inside the protein pocket of rhodopsin, a seven helix transmembrane protein, where it is covalently bound to Lys-296 via the protonated Schiff base linkage. In theoretical gas phase studies, there has been no consistent choice of how to terminate the covalent bond between the positively charge nitrogen in the protonated Schiff base and Lys-296. A single hydrogen, a methyl, and also an *n*-butyl group have been used as termination, and this particular choice appears to influence only slightly the excitation energy.[27,40] Due to the large size of the 11-*cis* retinal chromophore, smaller protonated Shiff base models have been mainly investigated theoretically, which differ in the length of the conjugated chain and the absence of methyl groups with respect to the complete chromophore.

The retinal models studied in this work are shown in Figure 1 and range from the minimal model (Figure 1A) to the full 11-*cis* retinal chromophore (Figure 1E). The atom labeling shown for the 11-*cis* chromophore is adopted also for the other models so that the *cis*-to-*trans* isomerization bond is always between the C_{11} and C_{12} atoms, with atom numbering increasing from the carbon to the nitrogen end. For the models without the β-ionone ring, we introduce the naming convention PSBx(y) where x and y are the number of double bonds and methyl groups, respectively. The PSB3(0) ($C_5H_6NH_2^+$) model (A) is the minimal model of the retinal chromophore and has already been extensively studied in the literature.[15,17,20,22,25,41] Since the methyl group at position C_{13} plays an important role in accelerating the isomerization process,[15,17] we also consider the PSB3(1) ($C_6H_8NH_2^+$) model (B), that is, the minimal model (A) with an added methyl group. The PSB4(1) ($C_8H_{10}NH_2^+$) model (C) has one additional double bond and has been previously studied without the methyl group using the CC and TDDFT methods.[29] The PSB5(1) ($C_{10}H_{12}NH_2^+$) model (D) has the full conjugated chain but is missing the β-ionone ring, and the complete 11-*cis* retinal chromophore (E) is here terminated with a single methyl group. With the exception of the 11-*cis* (E) chromophore, all other models are planar in the ground state. We note that a direct comparison with experiments is only possible for the vertical excitation energy of the 11-*cis* chromophore (E) since, to the best of our knowledge, none of the smaller models has been studied experimentally.

5. Vertical Excitation Energies

We compute the vertical excitation energies of the lowest singlet excited state (S_1) of all retinal models using the CASPT2, CC2, CCSD, VMC, and DMC approaches. The ground-state DFT/B3LYP geometries optimized with the cc-

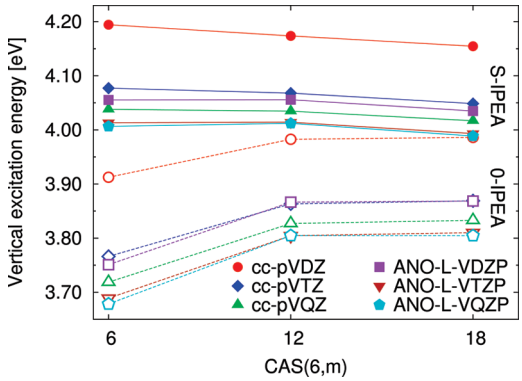

Figure 2. MS-CASPT2 vertical excitation (S_1) energies of the PSB3(0) model (A) computed with the standard IPEA Hamiltonian (S-IPEA, filled symbols) and with the IPEA shift set to zero (0-IPEA, empty symbols). The excitations are obtained with different basis sets and expansions CAS(6, *m*) of 6 electrons in *m* active orbitals. The ground-state DFT/B3LYP geometry is used.

pVDZ basis are used. The model E is optimized with no symmetry constraint (C_1), while the other models are planar and are optimized in either C_s or C_1 symmetry. The CASPT2 excitations are computed with the standard IPEA Hamiltonian (S-IPEA) and with the IPEA shift set to zero (0-IPEA), which was the default prior to MOLCAS 6.4, in order to be compatible with previous calculations in the literature.

5.1. Dependence on Basis Set and Other Parameters. Before comparing the relative performance of the different methods, we focus on the minimal model (A) and investigate the dependence of the excitations on the choice of the basis set and other parameters which may affect the calculations. We begin with the MS-CASPT2 approach and show in Figure 2 the vertical excitations obtained with the double (D), triple (T), and quadruple (Q) ζ basis sets from the cc-pVxZ and ANO-L-VxZP series. We correlate all 6 π electrons in the reference configuration and use a different number *m* of virtual π orbitals in the CAS(6,*m*) expansion. We note that single-state and MS-CASPT2 yield equivalent excitations for model A.

We observe that the ANO-L-VxZP series gives a faster convergence in the CASPT2 excitation energy than the correlated consistent basis. The excitations computed with the D basis are only 0.05 eV higher than the values obtained with the T and Q basis sets. On the other hand, in the cc-pVxZ series, the D excitations are 0.12 eV higher than the T values, which still differ from the Q results by 0.04 eV. The behavior of the CC2 and CCSD excitations with the basis set is not shown in the figure but parallels closely the one observed for the CASPT2 excitations. Therefore, since the ANO-L-VDZP basis set gives a good balance between accuracy and computational cost, it is used hereafter for all single-point CASPT2, CC2, and CCSD calculations.

We find that the CASPT2 results depend very strongly on the choice of the zero-order Hamiltonian. The difference between the excitation energies obtained with the standard IPEA Hamiltonian and the IPEA shift set to zero is independent of the basis set used and equal to about 0.3 eV when a CAS(6,6) is employed. As expected, the dependence on the particular zero-order Hamiltonian is reduced as the wave function is improved, and the difference between the excitations with and without the IPEA shift becomes 0.2 eV if the number of active π orbitals in the CAS is increased from 6 to 18. Finally, we observe that the vertical energies obtained with the IPEA shift set to zero are much more sensitive to the dimension of the CAS since they increase by 0.07−0.12 eV when *m* goes from 6 to 18, while the energies obtained with the standard IPEA Hamiltonian are quite stable and only decrease by about 0.02−0.04 eV.

Table 1. VMC and DMC Vertical Excitation (S_1) Energies (eV) of the PSB3(0) Model (A), Computed with Different Basis Sets and CAS Expansions Expressed on the Weighted-Averaged Natural Orbitals[a]

CAS(6, *m*)	Thr.	Det./CSF	Jastrow	basis	VMC	DMC
(6,6)	0.01	183/79	e−n, e−e	D+	4.32(1)	4.22(2)
(6,6)	0.02	101/47	e−n, e−e	D+	4.31(1)	4.20(2)
(6,6)	0.04	66/31	e−n, e−e	D+	4.31(1)	4.21(2)
(6,6)	0.08	23/10	e−n, e−e	D+	4.24(2)	4.19(2)
(6,6)[b]	0.08	23/10	e−n, e−e	D+	4.25(2)	4.21(2)
(6,6)[c]	0.08	23/10	e−n, e−e	D+	4.28(1)	4.16(2)
(6,6)	0.02	103/48	e−n, e−e	D	4.38(1)	4.29(2)
(6,6)	0.02	103/48	e−n, e−e	T′	4.34(1)	4.25(2)
(6,6)	0.02	103/48	e−n, e−e	Q′	4.34(1)	4.22(2)
(6,12)	0.02	152/66	e−n, e−e	D+	4.29(1)	4.22(2)
(6,18)	0.02	156/67	e−n, e−e	D+	4.29(1)	4.22(2)
(6,6)	0.02	101/47	e−n, e−e, e−e−n	D+	4.32(2)	4.24(2)

[a] The CAS(6,*m*) active space includes all 6 π electrons occupied in the reference configuration and *m* active π orbitals. The threshold on the expansion and the corresponding number of determinants and CSFs are also listed. Unless indicated, only the Jastrow and CI parameters are optimized. The ground-state DFT/B3LYP geometry is used. [b] Orbitals optimized including 40 external orbitals. [c] Orbitals optimized including 80 external orbitals.

In Table 1, we present an extensive QMC investigation for the minimal model (A) to assess how different ingredients in the trial wave function affect the excitation energy. The reference wave function is constructed from a CAS(6,6) expansion expressed on the weighted-averaged CASSCF natural orbitals in the D+ basis and truncated with a threshold of 0.02, where only the two-body Jastrow factor and CI coefficients are optimized in energy minimization in a SA fashion. Starting from this wave function, we investigate the effect of (*i*) changing the threshold on the CAS(6,6) expansion in the range 0.01−0.08, (*ii*) increasing the number of active π orbitals from 6 to 18 in the CAS(6,*m*) expansion, (*iii*) including an electron−electron−nuclear (e−e−n) term in the Jastrow factor in addition to the electron−nucleus (e−n) and electron−electron (e−e) components, (*iv*) optimizing the orbitals in a CAS(6,6) wave function with a threshold of 0.08 with both 40 and 80 external orbitals included in the optimization, and (*v*) using different basis sets (D, T′, and Q′). We find that the choice of basis has a significant effect on the QMC results as the VMC and DMC excitations computed with the D basis are higher by 0.06(2) and 0.09(3) eV than the corresponding D+ values. Since the use of the larger T′ and Q′ basis sets brings the excitations in closer agreement with the D+ results, we employ below the D+ basis set to compute the QMC excitations of all model chromophores. For this choice of basis, other ingredients in the trial wave function appear to have a smaller effect on the VMC and DMC excitation energies which range between 4.24(2) −4.32(2) and 4.16(2)−4.24(2) eV, respectively.

Table 2. Vertical Excitation (S_1) Energies (eV) of the Retinal Models[a]

		MS-CASPT2					
model	*n*	0-IPEA	S-IPEA	CC2	CCSD	VMC	DMC
(A) PSB3(0)	6	3.75	4.06	4.12	4.23	4.31(1)	4.20(2)
(B) PSB3(1)	6	3.86	4.18	4.20	4.37	4.52(2)	4.42(2)
(C) PSB4(1)	8	3.04	3.35	3.33	3.47	3.59(2)	3.47(2)
(D) PSB5(1)	10	2.58	2.87	2.82	2.95	3.08(2)	3.00(3)
(E) 11-*cis*	12	2.03[b]	2.30			2.59(3)	2.41(3)

[a] The MS-CASPT2 energies are computed both with the standard IPEA Hamiltonian (S-IPEA) and without the IPEA shift (0-IPEA). The CAS(*n*,*n*) expansion in the CASPT2 and QMC calculations includes all π electrons in the reference configuration and an equal number *n* of π orbitals. CASPT2 and CC employ the ANO-L-VDZP basis, and QMC the D+ basis. The ground-state DFT/B3LYP geometries are used. [b] Constant level shift of 0.2 au.

5.2. Results. We collect the vertical excitations of all retinal models computed using the MS-CASPT2, CC2, CCSD, VMC, and DMC methods on the ground-state DFT/B3LYP geometries in Table 2. The VMC and DMC excitations are obtained using wave functions where the Jastrow and CI parameters are optimized by energy minimization in a SA fashion and the threshold on the CSF expansion is 0.08 for the E model and 0.02 for all other models. It is evident that, for all models, the CASPT2 excitations obtained with the IPEA shift set to zero are at variance and significantly lower than the results obtained with all other theoretical methods. The use of the standard IPEA Hamiltonian raises the excitation energies of all models by as much as 0.3 eV and brings the CASPT2 values in close agreement with the CC2 results. The CCSD method yields excitations slightly higher by 0.11−0.17 eV than the CC2 and CASPT2 results obtained with the IPEA Hamiltonian. Finally, the VMC excitations are always higher by 0.1−0.2 eV than the DMC values which agree closely with the CCSD results.

For a comparison with experiments and previous theoretical work, we focus on the full 11-*cis* retinal chromophore (E) and collect the relevant results in Table 3. In line with previous calculations,[24,30,58] we find that the excitation energy of the retinal chromophore depends strongly on the method used to determine its ground-state structure. The sequence of BLYP, B3LYP, MP2, and CASSCF geometries corresponds to an increase of the degree of bond-length alternation and of the twisting of the β-ionone ring from −30° to −60° (see Figure 3). Stronger bond alternation and larger twisting angles correspond to larger excitations energies, and we find indeed an increase of 0.5 eV in the CASPT2 excitation both with and without the IPEA shift, when going from the BLYP to the CASSCF geometry. A comparison with CASPT2 geometries of planar retinal models indicates that DFT and MP2 ground-state structures represent a better model for the retinal chromophore in the gas phase as shown in Figure 6a and Figure SI-5 (Supporting Information) and already observed in ref 20. Even though discarding the CASSCF structures significantly reduces the spread in excitations, we still have an uncertainty of about 0.1 eV related to the choice of the particular DFT or MP2 geometry.

In Table 3, we present the single-state (SS) excitations in addition to results obtained with the MS-CASPT2 approach

Table 3. Single-State (SS) and MS-CASPT2, and DMC Vertical Excitations (S_1) Energies (eV) of the 11-*cis* Retinal (E) Chromophore[a]

Method	Geometry	E_{exc}	
SS-CASPT2		0-IPEA	S-IPEA
	DFT/BLYP	1.81[c]	2.12
	DFT/B3LYP	1.89[c]	2.20
	MP2	1.92[c]	2.24
	CASSCF[b]	2.30[c]	2.65[c]
MS-CASPT2			
	DFT/BLYP	1.96[c]	2.22
	DFT/B3LYP	2.03[c]	2.30
	MP2	2.08[c]	2.35
	CASSCF[b]	2.42[c]	2.72[c]
DMC/D+			
	DFT/BLYP	2.32(3)	
	DFT/B3LYP	2.41(3)	
Expt.[92]		2.05−2.34[d]	

[a] The experimental estimate is also listed. The geometries are optimized with the cc-pVDZ basis, and the CASPT2 calculations employ a CAS(12,12) expansion and the ANO-L-VDZP basis. [b] CASSCF(12,12)/6-31G(d) geometry from ref 27. [c] Constant level shift of 0.2 au. [d] Termination with two methyl groups, $-N(CH_3)_2^+$.

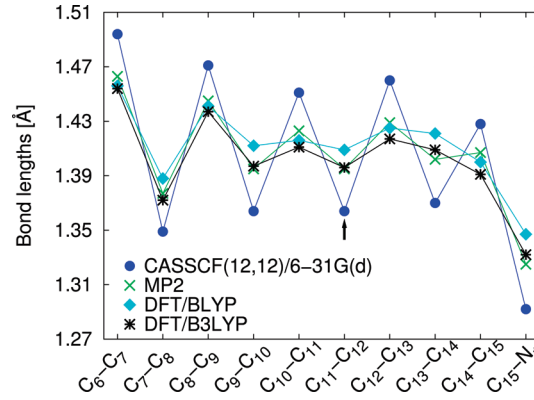

Figure 3. Ground-state bond lengths (Å) of the 11-*cis* chromophore (E) optimized using MP2, DFT/BLYP, and B3LYP and the cc-pVDZ basis. The CASSCF(12,12)/6-31G(d) geometry is from ref 27. The $C_5-C_6-C_7-C_8$ dihedral angles are −29.7°, −33.5°, −40.5°, and −68.8° in BLYP, B3LYP, MP2, and CASSCF, respectively.

as done so far in this section. As already mentioned, SS-CASPT2 and MS-CASPT2 give equivalent excitations within 0.01 eV for the smaller model A, as expected given the large gap of about 4 eV between the ground and excited states. However, as the size of the retinal model increases and the excitation decreases, SS-CASPT2 and MS-CASPT2 start to differ, and this discrepancy grows faster when no IPEA shift is employed. For the 11-*cis* model (E) and a gap of about 2 eV, the difference amounts to about 0.10 and 0.15 eV with and without the IPEA shift, respectively, and is independent of the ground-state geometry. Therefore, the choice of performing single- or multistate calculations within CASPT2 represents another internal parameter of the theory which affects the CASPT2 excitation in addition to the IPEA shift. We remark that, while MS-CASPT2 gives results which nicely parallel the DMC and CC excitations for all models, the difference between CASPT2 and other theories increases with system size if the single-state approach is used. The choice of the MS theory is our preference also for compat-

ibility with the CASPT2 excited-state geometrical optimizations presented in the next sections, where we employ the MS approach, as it is not known a priori whether the molecule will encounter a conical intersection region during relaxation.

We now compare our theoretical results with gas phase photodestruction experiments which are available for the 11-*cis* model terminated with two methyl groups.[92] The experimental absorption spectrum displays two main peaks at 2.05 eV (610 nm) and 3.18 eV (390 nm), which have been interpreted as the location of the vertical excitations to the two lowest singlet excited states (S_1 and S_2). The lowest-energy band (S_1) displays however a broad shoulder which has a secondary peak at 2.34 eV (530 nm) and is only about 20% lower in intensity than the absorption maximum at 2.05 eV. It has been previously suggested[33] that the vertical transition lies in the broad shoulder at higher energies and corresponds to the secondary peak at 2.34 eV. We further note that the adiabatic and not the vertical transition may be related to the lowest-energy feature at 2.05 eV. This interpretation of photodestruction experiments for retinal chromophores has in fact a parallel in the theoretical findings[66] and recent experimental reassessment[93] of photodestruction experiments of the photosensitive green fluorescent protein chromophore. We therefore report a range of energies between 2.05 and 2.34 eV as a more conservative experimental estimate of the vertical excitation of retinal chromophores. Our DMC, single-state, and MS-CASPT2 excitations are compatible with the experimental estimate, especially if we consider the remaining uncertainty on the ground-state DFT and MP2 geometries and the fact that we did not include vibrational effects. Setting the IPEA shift to zero moves the vertical CASPT2 excitation toward the lower end of the experimental range, namely, the possible location of the adiabatic transition, and the excitation even falls below the lower bound in the case of the single-state approach. We note that we could not perform CC calculations for the 11-*cis* model with the available codes and that the best CC2 result of 2.10 eV found in the literature[40] is about 0.20 eV lower than the CASPT2 excitation we compute on a similar B3LYP geometry. This discrepancy is rather puzzling since the CASPT2 and CC2 excitation energies agree rather well for all smaller models and could be due to the particular basis used in ref 40 or to the different response of CC2 and CASPT2 to the addition of the β-ionone ring missing in the smaller models.

6. In-Plane Geometrical Optimization

We optimize the in-plane excited-state geometries of the retinal chromophore models (A, B, C, D) using the CASSCF, MS-CASPT2, CC2, CCSD, and VMC approaches. We always follow the second root in the optimization and use two roots in the SA-CASSCF and MS-CASPT2 calculations as well as in the optimization of the VMC wave functions. The CAS expansion correlates all π electrons and an equal number of orbitals with the exception of models A and B, where we include more virtual orbitals to be consistent with previous calculations.[15] As shown in ref 22 for model A, a smaller active space of 6 electrons in 6 orbitals yields equivalent CASSCF results. We impose the planarity of the conjugated chain by constraining the optimization to C_s symmetry, and unless otherwise stated, we start the excited-state optimization from the DFT/B3LYP ground-state geometry.

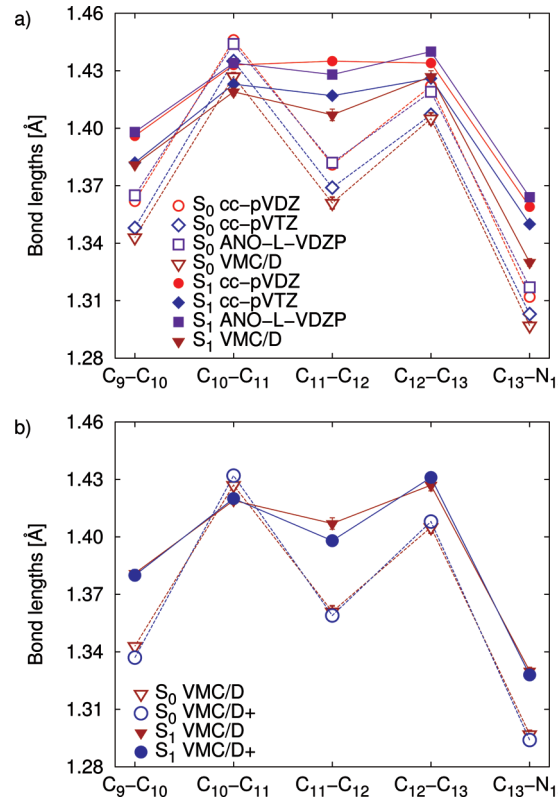

Figure 4. Bond lengths (Å) of the PSB3(0) model (A) optimized in the ground and excited states with the CASPT2 (panel a) and VMC (panel b) approaches and different basis sets. The CASPT2 geometries are computed with the cc-pVDZ, cc-pVTZ, and ANO-L-VDZP basis, and the VMC results with the D and D+ basis sets. In panel a, the VMC/D bond lengths are also shown for comparison. Planar symmetry is imposed.

6.1. Dependence on Basis Set and Other Parameters. In all geometrical optimizations, we employ the cc-pVDZ basis set. As shown in Figure 4a for the minimal model (A), the effect of using the larger cc-pVTZ basis set is to systematically shorten all ground- and excited-state CASPT2 bond lengths by about 0.010−0.015 Å without affecting the bond length pattern, as was also previously observed in ref 20. Differently from the case of the excitation energies, the ANO-L-VDZP basis yields comparable bond lengths to the cc-pVDZ value, which only disagree by 0.06 and 0.07 Å in the C_{11}−C_{12} and C_{12}−C_{13} excited-state bonds, respectively. A similar behavior as a function of the size of the basis set is also found for the CASSCF and DFT bond lengths, although the shortening in not as pronounced as for the CASPT2 results. In Figure 4b, we compare the VMC results obtained with the D and D+ basis sets, which are almost equal. Interestingly, the VMC results obtained with the D (cc-pVDZ) basis are very close to the CASPT2/cc-pVTZ results, so the presence of the Jastrow factor appears to compensate for the use of a smaller basis.

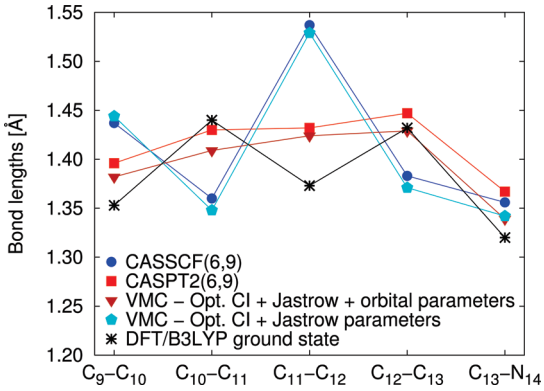

Figure 5. VMC bond lengths (Å) in the excited state of the PSB3(1) model (B) computed with two different wave functions. In one case, only the CI and Jastrow parameters are optimized within energy minimization in a state-average fashion while, in the other, all (orbital included) parameters are optimal. Planar symmetry is imposed.

The VMC geometrical optimization is very sensitive to the quality of the trial wave function as shown for model B in Figure 5. We start the optimization from the Franck−Condon region, and if we optimize only the Jastrow and CI coefficients within VMC, we obtain a VMC minimum which corresponds to the bond-inverted CASSCF geometry. On the other hand, if we include the orbital parameters in the VMC optimization, we obtain a very different VMC geometry which agrees with the minimum obtained by the other highly correlated approaches as shown below. Thus, in the VMC geometrical relaxation, we need to optimize all wave function parameters. We also note that preliminary calculations with DMC gradients indicate that the use of DMC does not mend the behavior of VMC when the DMC gradients are computed from wave functions with only optimal Jastrow and CI parameters.

6.2. Results. To understand how the geometry of the retinal chromophore is modified upon photoexcitation, we begin with the minimal model (A) and show in Figure 6a the ground-state bond lengths as obtained with the CASSCF, CASPT2, MP2, VMC, and DFT/B3LYP approaches. All methods agree in predicting a strong single−double bond-length alternation with a short, double bond between the central carbons. The MP2 and CASPT2 geometries are almost exactly equal since the ground state is dominated by a single configuration (89% weight) and CASPT2 is equivalent to MP2 for a single-reference CASSCF wave function. The DFT/B3LYP bond lengths deviate from the MP2 and CASPT2 values by at most 0.01 Å in the two single bonds. The VMC bond lengths are shorter by about 0.015 Å, and this can be explained as a basis set effect as discussed above. Only the CASSCF approach is at variance with the other approaches in the sense that it exhibits a greater bond length alternation, as has also been observed for larger retinal models.[20,26] The difference between CASSCF and the other approaches is on the order of 0.01−0.02 Å for model A but grows as the model becomes larger (see Figure SI-5, Supporting Information). In view of these results, we find that the DFT/B3LYP approach offers a good balance between performance and computational cost for the computation of the ground state structure.

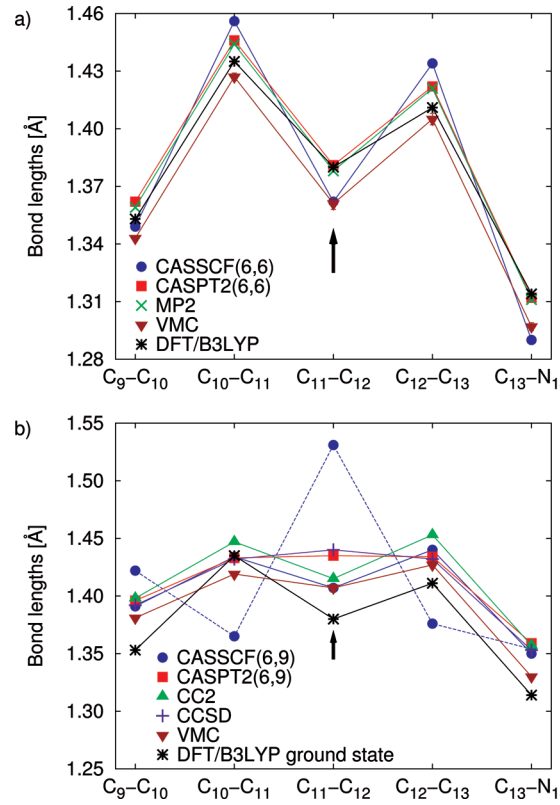

Figure 6. Bond lengths (Å) of the PSB3(0) model (A) optimized in the ground (panel a) and excited (panel b) states with the CC2, CCSD, CASSCF, CASPT2, and VMC methods. The DFT/B3LYP and MP2 ground states are also shown. The cc-pVDZ basis is used and planarity imposed. CASSCF displays two minima in the excited state.

The excited-state bond lengths of the minimal model (A) are shown in Figure 6b. The CASSCF approach exhibits two almost degenerate minima, while all other approaches yield only one minimum. The first CASSCF minimum (solid line) displays a lengthening of almost all bonds and a largely preserved bond-length pattern as compared to the ground state. The second CASSCF minimum (dashed line) is about 0.022 eV higher in energy than the other CASSCF minimum and displays a pronounced bond-length inversion with respect to the ground state. Importantly, we note that the first minimum is found when starting the optimization from the ground-state geometry, while we started from a geometry biased toward bond inversion to find the second one. In addition, regardless of the starting point, we only converge to a single CASSCF minimum, corresponding to the first minimum, if the ANO-L-VDZP basis set is used instead of the cc-pVDZ basis set. For the two CASSCF minima obtained with the cc-pVDZ basis, we report the wave function character and orbitals in the Supporting Information.

As for the other methods, we observe that most bond lengths become longer and more similar in the excited state. The CC2 and VMC structures largely preserve the short−long bond-length pattern of the ground state as observed for the first CASSCF minimum, while CASPT2 and CCSD give three middle bonds of almost equal length. At the CASPT2 level, we also investigated extensively the existence of a bond-inverted minimum by starting the excited-state optimization from geometries biased toward bond inversion but

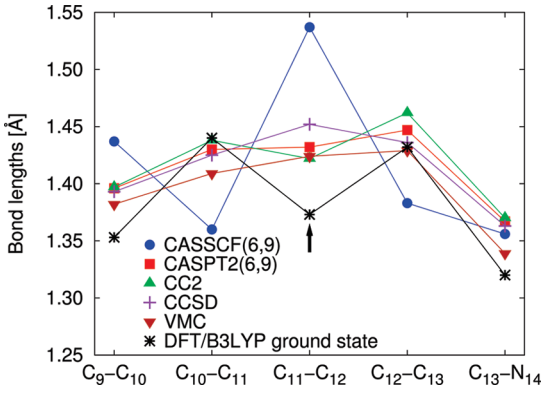

Figure 7. Bond lengths (Å) of the PSB3(1) model (B) optimized in the excited state with the CC2, CCSD, CASSCF, and CASPT2 methods. The DFT/B3LYP ground-state bond lengths are also shown. The cc-pVDZ basis is used and planar symmetry imposed. Differently from model A without the methyl (Figure 6), CASSCF only displays here one minimum.

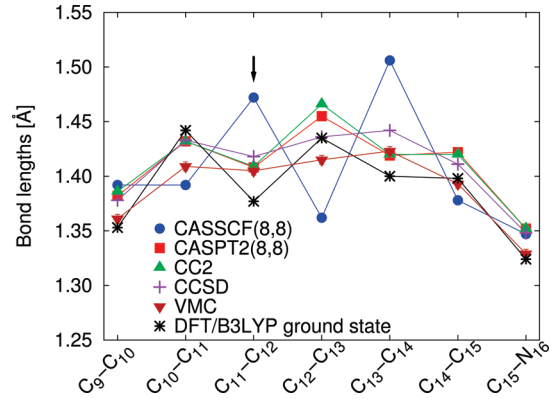

Figure 8. Bond lengths (Å) of the PSB4(1) model (C) optimized in the excited state with the CC2, CCSD, CASSCF, CASPT2, and VMC methods. The DFT/B3LYP ground-state bond lengths are also shown. The cc-pVDZ basis is used and planar symmetry imposed.

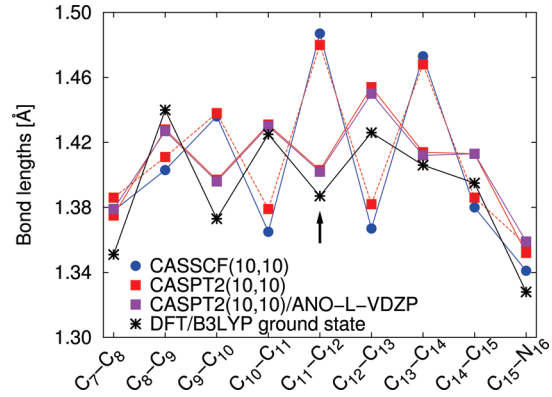

Figure 9. Bond lengths (Å) of the PSB5(1) model (D) optimized in the excited state with the CASSCF and CASPT2 methods and the cc-pVDZ basis. We also show the CASPT2/ANO-L-VDZP results. CASPT2 displays two minima in the excited state with the cc-pVDZ basis and only one minimum with the ANO-L-VDZP basis. The DFT/B3LYP ground-state bond lengths are also shown. Planar symmetry is imposed.

could not locate a second minimum. Our CASSCF and CASPT2 results are consistent with the study by Page and Olivucci[20] using the 6-31G(d) basis set.

Surprisingly, adding a methyl group to the minimal model (A) to generate model B has profound effects on the bond lengths, as shown in Figure 7. In particular, there is now only one CASSCF minimum which exhibits a pronounced bond length inversion as compared to the ground state and is at variance with the results obtained with all other approaches. The differences among the results obtained with the other methods is instead significantly smaller. The CC2 geometry of model B is similar to model A with a lengthening of most bonds and a largely preserved bond-length pattern with respect to the ground state. Similarly to model A, CASPT2 yields close to equal bond lengths for the three middle bonds, with the $C_{12}-C_{13}$ bond being the longest, while CCSD gives the middle $C_{11}-C_{12}$ bond as being slightly larger. The VMC minimum displays a similar bond length pattern as CASPT2 but shorter absolute bond lengths, which can be explained as a basis set effect as explained above.

When going to larger models, we find that CASSCF yields only one minimum where the short−long bond-length pattern is inverted with respect to the ground state as in the case of model B. In Figure 8, we show the excited-state bond lengths for model C and observe that the CASSCF minimum with bond-length inversion is at variance with all other approaches. The CASPT2 and CC2 are very close to each other and exhibit a largely preserved bond length pattern and overall lengthening of most bonds with respect to the ground state. The CCSD geometry displays no distinct bond-length pattern and an overall lengthening of most bonds, and the VMC gives a similar bond-length pattern as CCSD but shorter bond lengths as seen above.

In Figure 9, we show the excited-state bond lengths of model D, which has the full conjugated chain of the retinal chromophore and only misses the β-ionone ring. For this model, we only show the bond lengths obtained with the CASSCF and CASPT2 approaches. In addition, we also show CASPT2 results obtained with the ANO-L-VDZP basis set. As for models B and C, CASSCF gives a structure characterized by bond-length inversion with respect to the ground state. However, it is now the CASPT2 approach which gives two profoundly different minima. The first CASPT2 minimum (solid line) is similar to the CASPT2 geometry of model C with a preserved bond length pattern and overall lengthening of most bonds as compared to the ground state. The second CASPT2 minimum (dashed line) is very close to the CASSCF geometry and is about 0.045 eV higher in energy than the first CASPT2 minimum. Importantly, we note that the first CASPT2 minimum is found when starting from the ground-state geometry, while the second CASPT2 minimum is reached when starting from the CASSCF excited-state geometry. Moreover, the existence of this second minimum is dependent on the choice of the basis: The two CASPT2 minima obtained with the cc-pVDZ basis are also found when the 6-31G(d) basis set is used (not shown in the figure), while only the first CASPT2 minimum with no bond length inversion is obtained regardless of the starting geometry when the ANO-L-VDZP basis

set is used. These results seem to indicate that the bond-inverted CASPT2 structure is a spurious local minimum with no chemical significance, which is not reached when the optimization is started from the ground-state structure, that is, upon photoexcitation. We finally observe that a previous CASSCF and CASPT2 study by Page and Olivucci[20] using the 6-31G(d) basis set reports an excited-state CASPT2 structure of model D characterized by bond inversion. This finding can be easily explained by the fact that they started the CASPT2 geometrical optimization from the excited-state CASSCF minimum and were thus not able to reach the other minimum.

In summary, we see that the CASSCF excited-state geometries are at variance with the CASPT2, CC, and QMC results with the exception of the minimal model (A) where CASSCF displays two minimum structures, one of which is in agreement with the geometries obtained by the other approaches. The minimal model appears however to be a special case since the addition of a single methyl group in model B changes the picture and breaks the agreement between CASSCF and the other approaches. The inadequacy of CASSCF in describing in-plane excited structures of the retinal chromophore is also apparent from the results obtained for all the larger models.

7. Out-of-Plane Relaxation

7.1. Minimum Energy Paths. We determine the excited-state MEP of the retinal models B and C using the CASSCF and CASPT2 approaches. Ground- and excited-state CASSCF MEPs have previously been calculated for several retinal models,[15,16,18,22,33] and the common assumption is that the effect of dynamical correlation can be in part recovered by simply computing the CASPT2 energy on the final CASSCF geometries (CASPT2//CASSCF). Our aim here is to assess the validity of this assumption for the retinal chromophores by comparing the CASSCF and CASPT2 MEPs. To the best of our knowledge, the CASPT2 method has not been used to determine MEPs for the retinal models since CASPT2 energy gradients are substantially more expensive than CASSCF ones and still considered too costly for the routine investigation of these systems.[38,55] In the literature, we only found a CASPT2 study performing a constrained excited-state potential energy surface scan for the minimal model (A).[41]

The MEP calculations are performed using the steepest descent path optimization scheme implemented in MOLCAS 7.2 and described in ref 94. The procedure consists of a series of constrained geometrical optimizations in mass-weighted coordinates and yields the intrinsic reaction path. In each optimization, the potential energy is minimized on a hypersphere of a chosen radius, centered at a given reference structure. The CASSCF and CASPT2 ground-state geometries define the Franck−Condon point and initial reference structure for the corresponding MEP calculations. The radius of the hypersphere is either 0.06 or 0.1 au for model B and 0.1 au for model C. Upon convergence of the constrained geometrical optimization, the obtained minimum structure on the hypersphere is taken as new reference structure, and the procedure is iterated. As in the planar optimizations, the state averaging in the CASSCF and CASPT2 includes only the ground (S_0) and first excited state (S_1) since the next state is significantly higher in energy and does not play an active role (see Supporting Information).

We define the torsional angle θ as the $C_{10}-C_{11}-C_{12}-C_{13}$ dihedral angle and the torsional angle $\gamma = 180° - \phi$ where ϕ is the $C_{11}-C_{12}-C_{13}-C_{14}$ dihedral angle and γ is taken in the range from $-180°$ to $+180°$. Both torsional angles have a value of 0° in the ground state and indicate the deviation for planarity. These angles correspond to the torsional motion around the $C_{11}-C_{12}$ and $C_{12}-C_{13}$ bonds which are double and single in the ground state, respectively. We note that geometries corresponding to the angles (θ, γ) and $(-\theta, -\gamma)$ are equivalent since the molecules are planar in the ground state and there is no preferential direction for torsion.

In Figure 10, we show the results from the MEP calculation for model B and report the energies, the bond lengths for the formal double and single bonds along the conjugated chain, and the torsional angle θ for the central $C_{11}-C_{12}$ *cis* bond. The CASSCF MEP is characterized by two sequential modes. The initial relaxation is toward a planar structure similar to the CASSCF C_s minimum discussed above, which exhibits bond-length inversion with respect to the ground state, with the central $C_{11}-C_{12}$ bond being the longest in the excited state. This in-plane motion is followed by a torsion around the central bond toward an angle θ of about 65°, where a conical intersection region is encountered and the excited-state MEP is stopped. The CASSCF MEP is barrierless, while there is a small barrier of about 0.1 eV in the CASPT2//CASSCF energies.

The CASPT2 MEP is distinctly different from the CASSCF one even though the final outcome of the photoisomerization process is similar. The first difference is that the initial planar relaxation is toward a structure similar to the CASPT2 C_s minimum, which is therefore not characterized by bond inversion. The three middle bonds become almost equal, and the $C_{12}-C_{13}$ bond, which is long in the ground state, is the longest in the excited state. The subsequent torsional motion is around the central $C_{11}-C_{12}$ bond where we observe a plateau in the excited-state energy up to an angle θ of about 22°. When θ is about 17°, the three middle bonds begin to change dramatically: The central $C_{11}-C_{12}$ bond lengthens while the two neighboring bonds shorten, so their lengths become similar to those of the CASSCF MEP. The excited-state energy starts then decreasing at a faster pace, and the torsional motion continues toward $\theta \approx 69°$ where a conical intersection region is encountered and the excited-state MEP is stopped. A similar behavior is observed in the constraint excited-state optimization of the minimal model (A) in ref 41, where an energy plateau is observed for θ between 0° and 25°, followed by a sudden drop in the energy and change in geometry between 25° and 30°. In addition, studies on the minimal model (A) have found that conical intersection geometries obtained with CASSCF and CASPT2 are very similar.[19,20,23] This is consistent with the results obtained here as the CASSCF and CASPT2 MEPs show similar structures near the conical intersection.

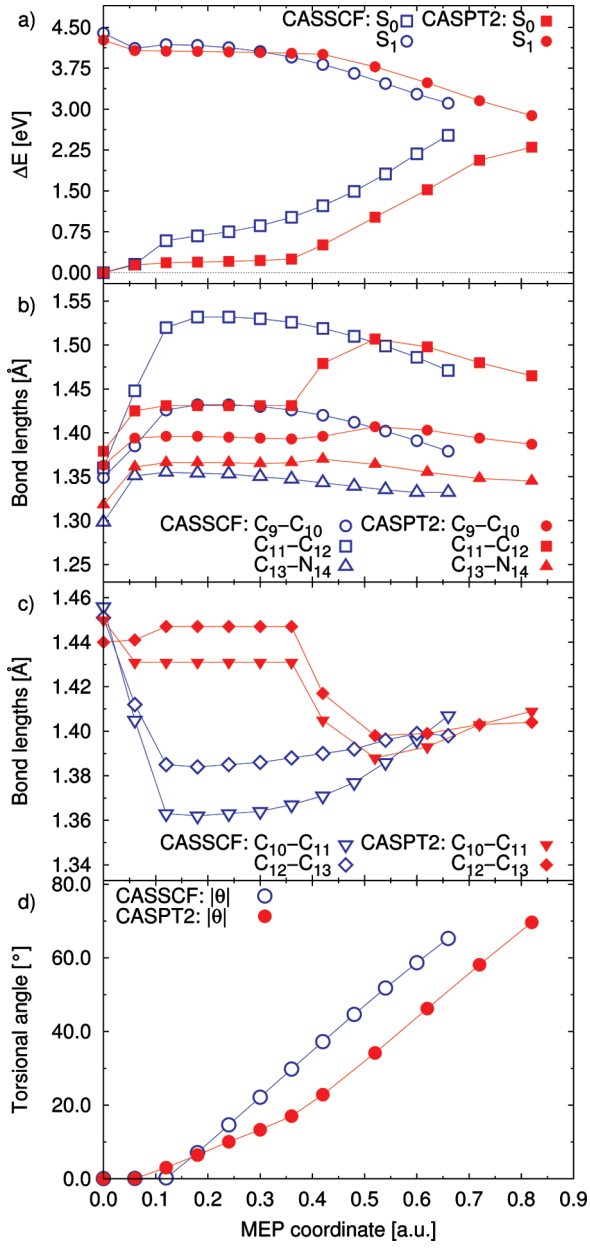

Figure 10. CASSCF and CASPT2 excited-state MEPs for the PSB3(1) model (B), obtained with a CAS(6,9) expansion and the cc-pVDZ basis. We report the CASPT2//CASSCF and CASPT2//CASPT2 ground- and excited-state energies (a), the bond lengths for formal double (b) and single bonds (c), and the absolute value of the torsional angle θ around the central $C_{11}-C_{12}$ bond (d). All energies are relative to the ground-state energies of the CASSCF and CASPT2 ground-state geometries, which are the starting point of the corresponding MEPs.

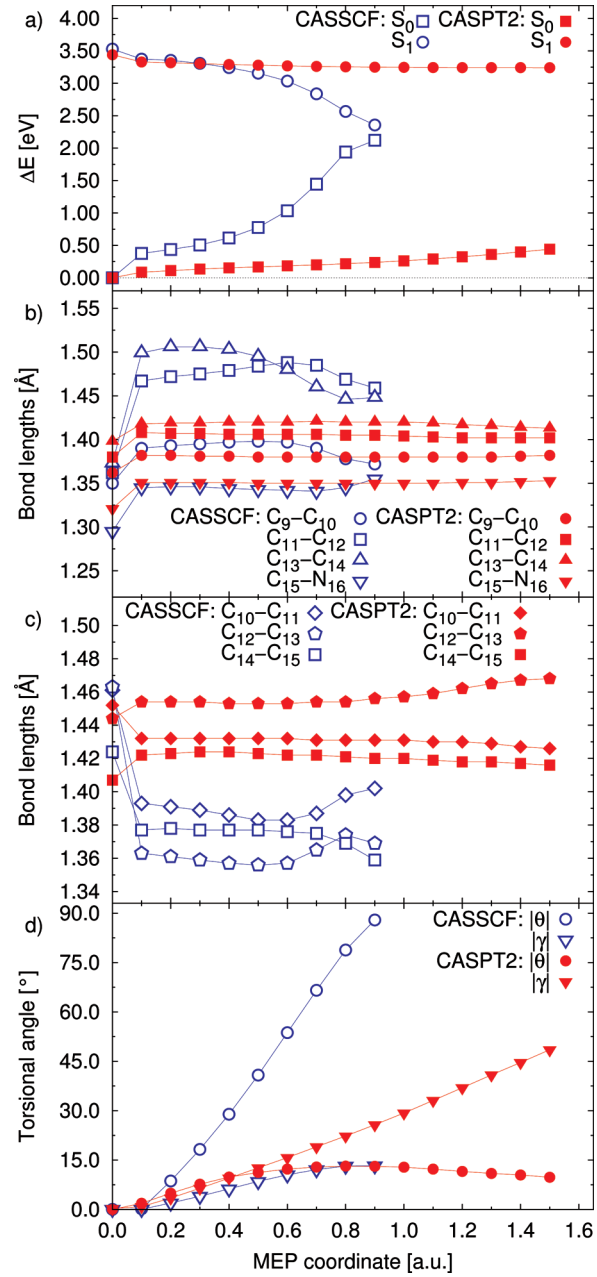

Figure 11. CASSCF and CASPT2 excited-state MEPs for the PSB4(1) model (C), obtained with a CAS(8,8) expansion and the cc-pVDZ basis. We report the CASPT2//CASSCF and CASPT2//CASPT2 ground- and excited-state energies (a), the bond lengths for formal double (b) and single bonds (c), and the absolute values of the torsional angles θ and γ around the $C_{11}-C_{12}$ and the $C_{12}-C_{13}$ bonds, respectively (d). For CASSCF, $\theta < 0°$ and $\gamma < 0°$, while, for CASPT2, $\theta > 0°$ and $\gamma < 0°$. All energies are relative to the ground-state energies at the CASSCF and CASPT2 ground-state geometries, which are the starting point for the corresponding MEPs.

To investigate the effect of lengthening the conjugated chain, we compute the MEP of model C, as shown in Figure 11. The CASSCF and CASPT2 approaches give a different isomerization mechanism, and the relevant torsional angles are not only θ around the $C_{11}-C_{12}$ bond (formal double) but also γ around the $C_{12}-C_{13}$ bond (formal single). The CASSCF MEP is similar to the one of model B and is characterized by two sequential modes, namely, an initial in-plane bond-length inversion followed by a torsional motion around the $C_{11}-C_{12}$ bond until the conical intersection region is encountered at $\theta \approx 88°$. There is also a small torsion around the $C_{12}-C_{13}$ bond with an angle $\gamma \approx 13°$ at the end of the MEP. Differently from model B, the CASPT2// CASSCF excited-state energies show no barrier.

The CASPT2 MEP is rather different from the CASSCF one. The initial relaxation is toward a planar structure which is similar to the CASPT2 C_s minimum and exhibits a largely preserved bond-length pattern with respect to the ground state

and an overall lengthening of most bonds. This in-plane motion is followed by a concerted increase of θ (also active in the CASSCF isomerization) and γ up to a MEP coordinate of 0.5 au. Beyond this point, γ keeps increasing while θ changes only slightly, so the molecule is twisting only around the $C_{12}-C_{13}$ bond (formal single), while all bond lengths remain almost constant. At a MEP coordinate of 1.5 au ($\gamma \approx -49°$), a barrier is encountered and the MEP optimization cannot proceed further. Both the ground- and excited-state energies vary very little along the whole MEP, and both states display a long plateau. At the final MEP coordinate, the excited-state energy is only 0.20 eV lower than the Franck−Condon point and the ground-state energy higher by about 0.44 eV, so the vertical excitation has decreased from 3.44 to 2.80 eV.

In order to compare the CASSCF and CASPT2 isomerization mechanisms with the CC2 results, we also perform straight geometrical excited-state optimization with all three approaches since the code we use to perform CC2 calculations does not have the capability of computing MEP. For consistency, all optimizations are started from the DFT/B3LYP ground-state geometries. For model B, all the approaches yield isomerization around the central $C_{11}-C_{12}$ bond and proceed toward the same final point in the conical intersection region. However, from the CASSCF and CASPT2 MEP results, we know that the isomerization proceeds rather differently even though the final structures are equivalent. Therefore, we cannot infer too much about the behavior of CC2 from the agreement of the method on the final structure of model B but proceed with model C, where the final outcomes of the CASSCF and CASPT2 MEP are distinctively different.

We show the optimal CC2 and CASPT2 excited-state structures of model C in Figure 12. We observe that CC2 isomerizes around the $C_{12}-C_{13}$ bond as CASPT2, while CASSCF is consistent with the MEP behavior and yields isomerization around the $C_{11}-C_{12}$ bond (not shown in the figure). The CASPT2 optimal geometry has a torsional angle $\gamma = 43.6°$ and is energetically between the MEP geometries at 1.3 and 1.4 au. Even though the isomerization is around the same bond, the optimal CC2 torsional angle of $\gamma = 100.1°$ is however significantly different from the CASPT2 value. To understand this difference, we investigate the possible existence of a barrier in the CASPT2 potential energy surface and perform a constrained excited-state geometrical optimization in CASPT2 by varying the angle γ between 45° and 85°. The resulting excited-state energies are shown in Figure 13 and display a small barrier of about 0.03 eV. If we perform an excited-state CASPT2 optimization starting from the constrained structure just beyond the barrier, we recover a minimum excited-state structure which has a torsional angle of $\gamma = 112.7°$ (Figure 12c) and is in much closer agreement with the CC2 optimal geometry. The CASPT2 excited-state energy is only 0.09 eV lower than the value for the minimal structure at $\gamma = 43.6°$. An analysis of the CASPT2 geometries along the constrained path of Figure 13 reveals that the origin of the barrier is due to steric interactions of the methyl group with the nearby hydrogens since the main difference between the geometries before and after the barrier is a small rotation of the methyl group. We also note that a previous CC2 investigation on model C without the methyl group [PSB4(0)] found a small barrier of 0.01 eV at $\gamma \approx 30°$ and an absolute minimum at about 100°.[29] Therefore, the apparent presence/absence of a barrier in the CASPT2/CC2 optimization may possibly be due to the particular geometrical optimization algorithm used in the different codes or to slightly different initial configurations in the optimization procedure.

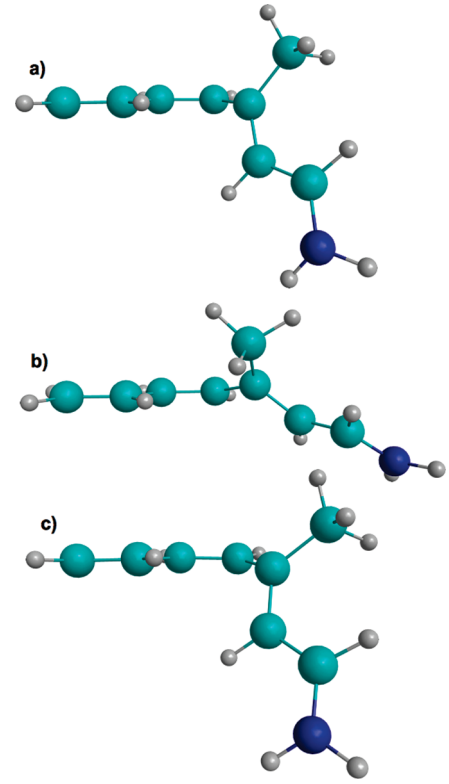

Figure 12. CC2 (a) and CASPT2 (b) excited-state optimal structures of the PSB4(1) model (C), obtained by starting the optimization from the DFT/B3LYP ground-state geometry. The CC2 torsional angles are $\gamma = 100.1°$ and $\theta = 2.6°$, while CASPT2 yields $\gamma = 43.6°$ and $\theta = -10.5°$. The CASPT2 structure (c) is obtained by starting the optimization from the constrained structure just beyond the barrier ($\gamma = 75°$) in Figure 13 and has angles $\gamma = 112.7°$ and $\theta = 8.1°$.

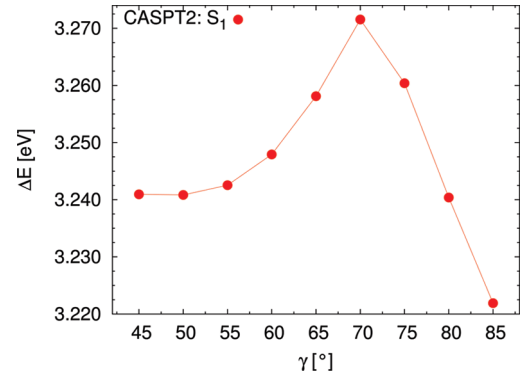

Figure 13. CASPT2 excited-state energies of the PSB4(1) model (C) optimized at constrained torsional angles, γ, from 45° to 85°. The energy is shown relative to the ground-state value at the starting point of the CASPT2 MEP (Figure 11). A CAS(8,8) expansion and the cc-pVDZ basis set are used.

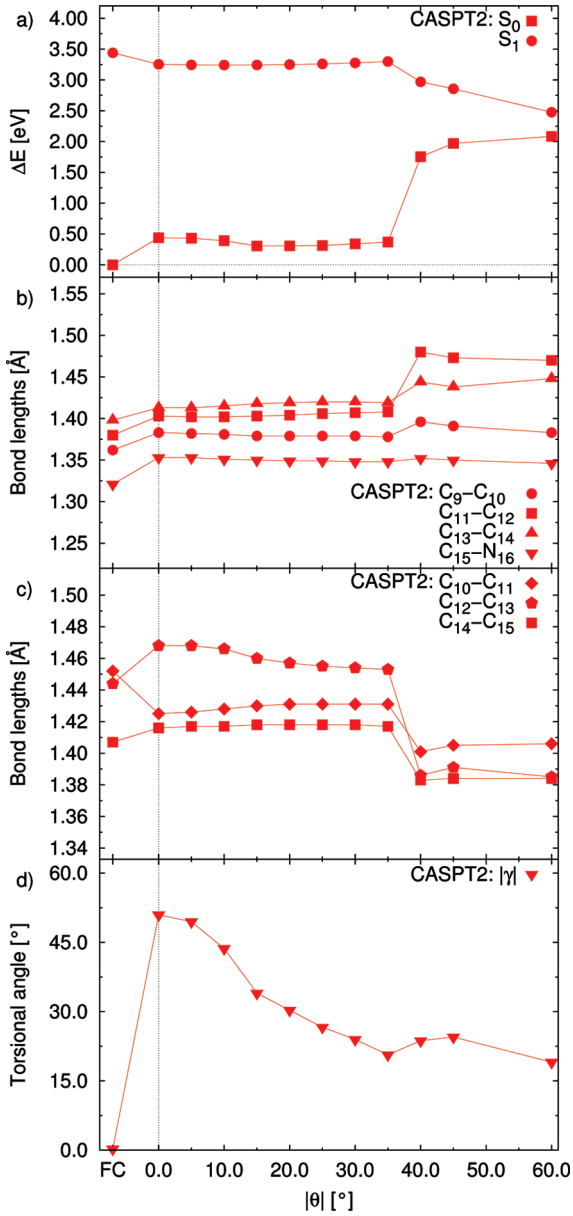

Figure 14. CASPT2 excited-state optimization of the PSB4(1) model (C) at constrained torsional angles, θ, from 0° to 60°. We report the CASPT2//CASPT2 ground- and excited-state energies (a), the bond lengths for formal double (b) and single bonds (c), and the absolute value of the torsional angle γ around the $C_{12}-C_{13}$ bond (d). The quantities computed at the CASPT2 Franck−Condon (FC) point are also shown in all panels. A CAS(8,8) expansion and the cc-pVDZ basis set are used. For the torsional angle, $\theta < 0°$ and $\gamma > 0°$.

7.2. Reactive versus Nonreactive Paths. The CASPT2 MEP of the retinal model C gives isomerization around a single bond, does not lead to a conical intersection region, and corresponds to a nonreactive path. To investigate whether a rotation around a double bond may give a reactive path and lead to a photoproduct, we optimize the excited-state CASPT2 geometry of model C at constrained torsional angles, θ, around the $C_{11}-C_{12}$ *cis* bond and show the results in Figure 14.

At $\theta = 0°$, the molecule is unstable toward single-bond rotation, which is not surprising since the CASPT2 MEP gives isomerization around the same single bond and is always characterized by small values of the angle θ (less than 10°). The resulting constrained geometry has an angle γ of about 51° and is in fact very similar to the last point of the CASPT2 MEP. If we increase θ from 0° to 35°, the angle γ diminishes while the bond lengths become closer to the values in the initial part of the CASPT2 MEP. Concurrently, the excited-state energy rises and displays a small barrier of about 0.06 eV, which peaks at $\theta = 35°$. The barrier is overcome at $\theta = 40°$, where we suddenly observe bond inversion and a large increase in the ground-state energy and a decrease in the excited-state energy. The degree of bond inversion is however not as pronounced as in the CASSCF MEP, and the geometries are characterized by a larger residual rotation around the single bond. If we further increase θ, the excitation energy continues to decrease, and we encounter a conical intersection region. The CASPT2 isomerization around the double bond corresponds therefore to a reactive path which is characterized by a small barier and eventually leads to a conical intersection region whose topology is rather similar to the CASSCF one.

To assess the behavior of the CC approach, we also perform constrained CC2 optimization around the double bond. The CC2 optimization at small values of θ leads to a single-bond rotation with very large values of γ (greater than 90°). This is compatible with the previous observation that the small steric barrier observed in CASPT2 (see Figure 13) is practically absent in the single-bond isomerization at the CC2 level. If we increase θ up to 60° and always start the optimization from the optimal constrained geometry at the previous angle, we cannot sufficiently reverse the large rotation around the single bond and the excited-state energy increases instead of decreasing. To assess the existence of a path leading to a conical intersection, we follow therefore a different procedure and simply compute the CC2 energies on the optimal constrained CASPT2 geometries of Figure 14. We find that the ground- and excited-state CC2 energies are in very good agreement with the CASPT2 values up to $\theta = 45°$. As expected and also discussed in ref 37, CC2 encounters convergence problems at larger values of θ as the system is approaching the conical intersection region. Consequently, the use of CC2 confirms the existence of a reactive path which corresponds to double-bond rotation, displays a small barrier, and leads to lower excited-state energies. However, the approach is not suitable for following the system through the conical intersection toward a photoproduct.

8. Discussion and Conclusions

We have presented a systematic investigation of model retinal chromophores in the gas phase with special emphasis on geometrical relaxation in the excited state. One aim of the work is to assess the relative performance of very diverse computational approaches as CASSCF, CASPT2, CC, and QMC in describing conformational changes in the excited states. The other major goal is to determine the validity of the generally accepted picture resulting from CASSCF calculations that the excited-state relaxation of retinal chromophores proceeds via bond inversion and torsional motion around formal double bonds. Differently from previous

studies, we employ approaches such as CASPT2 and QMC, which are superior to CASSCF as they offer a balanced description of both dynamical and static correlations.

We have also computed the vertical excitations of the retinal models using CASPT2, CC, and QMC, and we begin our discussion with a few comments on these results. We find that the CC and DMC methods give similar excitations for all retinal models and that the CASPT2 excitations are quite sensitive to the internal parameters of the theory. In particular, the excitations computed with the IPEA zero-order Hamiltonian are in close agreement with the CC and DMC values, while resorting to the original CASPT2 formulation lowers the excitations by as much as 0.3 eV. The IPEA Hamiltonian was developed to give on average more accurate excitations,[79] and its use is here corroborated by the good agreement with other highly correlated approaches. We also find that the IPEA excitations are more robust as they converge faster with the size of the CAS expansion and are less sensitive to the use of a single- or multistate approach.

For a comparison with experiments, we consider the 11-*cis* chromophore where gas phase photodestruction spectroscopy experiments are available.[92] To interpret the complex absorption spectrum of retinal chromophores, we follow the recent reassessment of similar experiments on a different chromophore[93] and suggest that the lowest-energy peak may correspond to the adiabatic transition while the vertical lies in the broad shoulder around 2.34 eV. Our CASPT2 and DMC vertical excitations computed on the DFT and MP2 ground-state geometries span an energy range of 2.2−2.4 eV, which is consistent with this experimental estimate especially given that we did not include vibrational effects which are strong in this system. The excitations computed on the CASSCF geometry are instead significantly higher but can be discarded as our CASPT2 optimizations of planar retinal models show that DFT and MP2 give more accurate geometries than the CASSCF approach.

We discuss now the core of our work and analyze the performance of the various theoretical approaches in describing the excited-state relaxation of retinal models. Our in-plane optimization of the retinal chromophores indicates that the excited-state structures optimized with CASPT2, CC2, CCSD, and VMC agree rather closely, while they are at variance with the CASSCF geometries. The CASSCF approach gives strong bond inversion in the excited state, which is not observed when optimizing the structures with the other approaches. According to CASPT2, CC, and VMC, photoexcitation weakens all bonds, which stretch and become partly more similar in length while preserving the general bond-length pattern of the ground state. To investigate a nontrivial out-of-plane relaxation, we need to consider a chromophore larger than the model with three double bonds (A or B) since we find that model B isomerizes around the central bond at both the CASPT2 and CASSCF levels, even though the initial skeletal relaxation proceeds rather differently in the two approaches. Therefore, we investigate the minimal energy path for the out-of-plane motion of model C with four double bonds and find that excited-state relaxation at the CASPT2 level proceeds preferentially via a torsional motion around a bond which is formally single in the ground state in agreement with the previous CC calculations by Send and Sundholm.[29,31,35,37] This torsional motion stops at an angle of about 45° and does not lead to a conical intersection region. On the other hand, in the CASSCF approach, bond inversion is followed by torsion around the *cis* bond, and the molecule is immediately funneled into a conical intersection region from where isomerization can proceed toward the *trans* product. To investigate the existence of a reactive path at the CASPT2 level, we also consider the constrained excited-state optimization of model C around the *cis* double bond and find a small barrier to isomerization at rather large angles of rotation. Beyond this barrier, the model finally reaches the conical intersection region similarly to the CASSCF approach.

In summary, our CASPT2 results support the picture of a very flexible retinal chromophore in the excited state, where photoexcitation lengthens all bonds so that torsional motion around nearly any bond may contribute to the dynamics. These findings are consistent with recent CC studies[37] which show that retinal models in the excited state have small or vanishing torsional barriers around both formal single and double bonds. This picture must be contrasted to the results of CASSCF calculations, which give a stiff chromophore that can only twist around formal double bonds. The flexibility of the excited chromophore in the gas phase observed in CASPT2 and CC calculations is also compatible with the observation in solution experiments of the existence of multiple minima possibly corresponding to different torsional conformations.[67] Moreover, it has been proposed that the multiexponential decays observed in solution are related to the possible presence of multiple excited-state paths, some of which are reactive and lead to the photoproduct via the crossing of a conical intersection region, while others are nonreactive, do not lead to conical intersection, and are dominant in solution.[67] This interpretation is compatible with our observation of torsional motion around formal single bonds, which is favored starting from the Franck−Condon region, stops at intermediate angles, and does not lead to photoproducts via a conical intersection.

Finally, our results demonstrate the importance of including a balanced description of dynamical and static correlation in the computation of the excited-state gradients. The favorable comparison with the CASPT2 approach indicates that the CC2 method is a useful tool for the study of retinal systems (at least far from the conical intersection region) and that QMC can give accurate gradients when all parameters in the wave function are optimized in energy minimization. Our results raise serious concerns about the common use of the CASSCF approach to investigate the geometrical relaxation of retinal systems and show that computing single-point CASPT2 excitations on CASSCF geometries to partially include the neglected dynamical correlation is generally not a valid procedure to obtain reliable potential energy surfaces. In conclusion, our findings call for a reinvestigation of the photoisomerization mechanism of retinal chromophores in the gas phase as well as in the protein environment with higher-level methods than the CASSCF approach.

Acknowledgment. We thank Massimo Olivucci, Ivano Tavernelli, Robert Send, and Saverio Moroni for useful discussions. We acknowledge the support from the Stichting Nationale Computerfaciliteiten (NCF-NWO) for the use of the SARA supercomputer facilities.

Supporting Information Available: SA-CASSCF and SS-CASPT2 excitations of all models; basis set convergence of the SA-CASSCF and CC energies of the PSB3(0) model (A); character of the excited-state CASSCF wave function and orbitals computed at the ground-state B3LYP, excited-state CASPT2, and two excited-state CASSCF planar minima of the PSB3(0) model (A); ground-state bond lengths of the PSB5(1) model (C); CASPT2 energies computed along the out-of-plane excited-state relaxation paths of models PSB3(1) (A) and PSB4(1) (B) and obtained with a state average over three states in the CASSCF and CASPT2 calculations; ground- and excited-state coordinates of all retinal models. This material is available free of charge via the Internet at http://pubs.acs.org.

References

(1) Wald, G. *Science* **1968**, *162*, 230–239.

(2) Okada, T.; Sugihara, M.; Bondar, A.-N.; Elstner, M.; Entel, P.; Buss, V. *J. Mol. Biol.* **2004**, *342*, 571–583.

(3) Kandori, H.; Shichida, Y.; Yoshizawa, T. *Biochemistry (Moscow)* **2001**, *66*, 1483–1498.

(4) Schoenlein, R. W.; Peteanu, L. A.; Mathies, R. A.; Shank, C. V. *Science* **1991**, *254*, 412–415.

(5) Kandori, H.; Katsuta, Y.; Ito, M.; Sasabe, H. *J. Am. Chem. Soc.* **1995**, *117*, 2669–2670.

(6) Becker, R. S.; Freedman, K. *J. Am. Chem. Soc.* **1985**, *107*, 1477–1485.

(7) Kim, J. E.; Tauber, M. J.; Mathies, R. A. *Biochemistry* **2001**, *40*, 13774–13778.

(8) Kandori, H.; Furutani, Y.; Nishimura, S.; Shichida, Y.; Chosrowjan, H.; Shibata, Y.; Mataga, N. *Chem. Phys. Lett.* **2001**, *334*, 271–276.

(9) Kobayashi, T.; Saito, T.; Ohtani, H. *Nature* **2001**, *414*, 531–534.

(10) Herbst, J.; Heyne, K.; Diller, R. *Science* **2002**, *297*, 822–825.

(11) McCamant, D. W.; Kukura, P.; Mathies, R. A. *J. Phys. Chem. B* **2005**, *109*, 10449–10457.

(12) Kukura, P.; McCamant, D. W.; Yoon, S.; Wandschneider, D. B.; Mathies, R. A. *Science* **2005**, *310*, 1006–1009.

(13) Kukura, P.; McCamant, D. W.; Mathies, R. A. *Annu. Rev. Phys. Chem.* **2007**, *58*, 461–488.

(14) Kennis, J. T.; Groot, M.-L. *Curr. Opin. Struct. Biol.* **2007**, *17*, 623–630.

(15) Garavelli, M.; Celani, P.; Bernardi, F.; Robb, M. A.; Olivucci, M. *J. Am. Chem. Soc.* **1997**, *119*, 6891–6901.

(16) Garavelli, M.; Vreven, T.; Celani, P.; Bernardi, F.; Robb, M. A.; Olivucci, M. *J. Am. Chem. Soc.* **1998**, *120*, 1285–1288.

(17) Garavelli, M.; Bernardi, F.; Olivucci, M.; Vreven, T.; Klein, S.; Celani, P.; Robb, M. A. *Faraday Discuss.* **1998**, *110*, 51–70.

(18) González-Luque, R.; Garavelli, M.; Bernardi, F.; Merchán, M.; Robb, M. A.; Olivucci, M. *Proc. Natl. Acad. Sci. U.S.A.* **2000**, *97*, 9379–9384.

(19) De Vico, L.; Page, C. S.; Garavelli, M.; Bernardi, F.; Basosi, R.; Olivucci, M. *J. Am. Chem. Soc.* **2002**, *124*, 4124–4134.

(20) Page, C. S.; Olivucci, M. *J. Comput. Chem.* **2003**, *24*, 298–309.

(21) Wanko, M.; Garavelli, M.; Bernardi, F.; Niehaus, T. A.; Frauenheim, T.; Elstner, M. *J. Chem. Phys.* **2004**, *120*, 1674–1692.

(22) Fantacci, S.; Migani, A.; Olivucci, M. *J. Phys. Chem. A* **2004**, *108*, 1208–1213.

(23) Serrano-Andrés, L.; Merchán, M.; Lindh, R. *J. Chem. Phys.* **2005**, *122*, 104107.

(24) Wanko, M.; Hoffmann, M.; Strodel, P.; Koslowski, A.; Thiel, W.; Neese, F.; Frauenheim, T.; Elstner, M. *J. Phys. Chem. B* **2005**, *109*, 3606–3615.

(25) Tavernelli, I.; Röhrig, U. F.; Rothlisberger, U. *Mol. Phys.* **2005**, *103*, 963–981.

(26) Blomgren, F.; Larsson, S. *J. Comput. Chem.* **2005**, *26*, 738–742.

(27) Cembran, A.; Gonzalez-Luque, R.; Altoe, P.; Merchan, M.; Bernardi, F.; Olivucci, M.; Garavelli, M. *J. Phys. Chem. A* **2005**, *109*, 6597–6605.

(28) Aquino, A. J. A.; Barbatti, M.; Lischka, H. *ChemPhysChem* **2006**, *7*, 2089–2096.

(29) Send, R.; Sundholm, D. *J. Phys. Chem. A* **2007**, *111*, 27–33.

(30) Send, R.; Sundholm, D. *Phys. Chem. Chem. Phys.* **2007**, *9*, 2862–2867.

(31) Send, R.; Sundholm, D. *J. Phys. Chem. A* **2007**, *111*, 8766–8773.

(32) Barbatti, M.; Granucci, G.; Persico, M.; Ruckenbauer, M.; Vazdar, M.; Eckert-Maksić, M.; Lischka, H. *J. Photochem. Photobiol., A* **2007**, *190*, 228–240.

(33) Cembran, A.; González-Luque, R.; Serrano-Andrés, L.; Merchán, M.; Garavelli, M. *Theor. Chem. Acc.* **2007**, *118*, 173−183.

(34) Weingart, O. *J. Am. Chem. Soc.* **2007**, *129*, 10618–10619.

(35) Send, R.; Sundholm, D. *J. Mol. Model.* **2008**, *14*, 717–726.

(36) Szymczak, J. J.; Barbatti, M.; Lischka, H. *J. Chem. Theory Comput.* **2008**, *4*, 1189–1199.

(37) Send, R.; Sundholm, D.; Johansson, M. P.; Pawłowski, F. *J. Chem. Theory Comput.* **2009**, *5*, 2401–2414.

(38) Schapiro, I.; Weingart, O.; Buss, V. *J. Am. Chem. Soc.* **2009**, *131*, 16–17.

(39) Szymczak, J. J.; Barbatti, M.; Lischka, H. *J. Phys. Chem. A* **2009**, *113*, 11907–11918.

(40) Zaari, R. R.; Wong, S. Y. *Chem. Phys. Lett.* **2009**, *469*, 224–228.

(41) Keal, T.; Wanko, M.; Thiel, W. *Theor. Chem. Acc.* **2009**, *123*, 145–156.

(42) Warshel, A. *Nature* **1976**, *260*, 679–683.

(43) Warshel, A.; Barboy, N. *J. Am. Chem. Soc.* **1982**, *104*, 1469–1476.

(44) Liu, R. S.; Asato, A. E. *Proc. Natl. Acad. Sci. U.S.A.* **1985**, *82*, 259–263.

(45) Hayashi, S.; Tajkhorshid, E.; Schulten, K. *Biophys. J.* **2003**, *85*, 1440–1449.

(46) Andruniów, T.; Ferré, N.; Olivucci, M. *Proc. Natl. Acad. Sci. U.S.A.* **2004**, *101*, 17908–17913.

(47) Röhrig, U. F.; Guidoni, L.; Laio, A.; Frank, I.; Rothlisberger, U. *J. Am. Chem. Soc.* **2004**, *126*, 15328–15329.

(48) Röhrig, U. F.; Guidoni, L.; Rothlisberger, U. *ChemPhysChem* **2005**, *6*, 1836–1847.

(49) Hoffmann, M.; Wanko, M.; Strodel, P.; Konig, P. H.; Frauenheim, T.; Schulten, K.; Thiel, W.; Tajkhorshid, E.; Elstner, M. *J. Am. Chem. Soc.* **2006**, *128*, 10808–10818.

(50) Coto, P. B.; Strambi, A.; Ferré, N.; Olivucci, M. *Proc. Natl. Acad. Sci. U.S.A.* **2006**, *103*, 17154–17159.

(51) Sugihara, M.; Hufen, J.; Buss, V. *Biochemistry* **2006**, *45*, 801–810.

(52) Sekharan, S.; Sugihara, M.; Buss, V. *Angew. Chem., Int. Ed.* **2007**, *46*, 269–271.

(53) Bravaya, K.; Bochenkova, A.; Granovsky, A.; Nemukhin, A. *J. Am. Chem. Soc.* **2007**, *129*, 13035–13042.

(54) Fujimoto, K.; Hayashi, S.; Hasegawa, J.-y.; Nakatsuji, H. *J. Chem. Theory Comput.* **2007**, *3*, 605–618.

(55) Frutos, L. M.; Andruniów, T.; Santoro, F.; Ferré, N.; Olivucci, M. *Proc. Natl. Acad. Sci. U.S.A.* **2007**, *104*, 7764–7769.

(56) Altun, A.; Yokoyama, S.; Morokuma, K. *Photochem. Photobiol.* **2008**, *84*, 845–854.

(57) Altun, A.; Yokoyama, S.; Morokuma, K. *J. Phys. Chem. B* **2008**, *112*, 6814–6827.

(58) Altun, A.; Yokoyama, S.; Morokuma, K. *J. Phys. Chem. B* **2008**, *112*, 16883–16890.

(59) Altun, A.; Yokoyama, S.; Morokuma, K. *J. Phys. Chem. A* **2009**, *113*, 11685–11692.

(60) Tomasello, G.; Olaso-González, G.; Altoeà, P.; Stenta, M.; Serrano-Andreás, L.; Merchaán, M.; Orlandi, G.; Bottoni, A.; Garavelli, M. *J. Am. Chem. Soc.* **2009**, *131*, 5172–5186.

(61) Hayashi, S.; Tajkhorshid, E.; Schulten, K. *Biophys. J.* **2009**, *96*, 403–416.

(62) Schautz, F.; Filippi, C. *J. Chem. Phys.* **2004**, *120*, 10931–10941.

(63) Schautz, F.; Buda, F.; Filippi, C. *J. Chem. Phys.* **2004**, *121*, 5836–5844.

(64) Cordova, F.; Doriol, L. J.; Ipatov, A.; Casida, M. E.; Filippi, C.; Vela, A. *J. Chem. Phys.* **2007**, *127*, 164111.

(65) Tapavicza, E.; Tavernelli, I.; Rothlisberger, U.; Filippi, C.; Casida, M. E. *J. Chem. Phys.* **2008**, *129*, 124108.

(66) Filippi, C.; Zaccheddu, M.; Buda, F. *J. Chem. Theory Comput.* **2009**, *5*, 2074–2087.

(67) Zgrablić, G.; Haacke, S.; Chergui, M. *J. Phys. Chem. B* **2009**, *113*, 4384–4393.

(68) Jensen, F. *Introduction to Computational Chemistry*, 2nd ed.; John Wiley and Sons Ltd: Chichester, U.K., 2007.

(69) Foulkes, W. M. C.; Mitas, L.; Needs, R. J.; Rajagopal, G. *Rev. Mod. Phys.* **2001**, *73*, 33–83.

(70) Nightingale, M. P.; Melik-Alaverdian, V. *Phys. Rev. Lett.* **2001**, *87*, 043401.

(71) Umrigar, C. J.; Toulouse, J.; Filippi, C.; Sorella, S.; Hennig, R. G. *Phys. Rev. Lett.* **2007**, *98*, 110201.

(72) Filippi, C.; Umrigar, C. J. *Phys. Rev. B* **2000**, *61*, R16291–R16294.

(73) Attaccalite, C.; Sorella, S. *Phys. Rev. Lett.* **2008**, *100*, 114501.

(74) We find that varying the cutoff parameter ε between 10^{-2} and 1.0 does not lead to appreciable changes in the root-mean-square fluctuations of the VMC forces (σ). On the other hand, the use of $\varepsilon = 10^{-3}$ and smaller values results in a significant increase in σ for the systems studied in this paper.

(75) Karlström, G.; Lindh, R.; Malmqvist, P.-Å.; Roos, B. O.; Ryde, U.; Veryazov, V.; Widmark, P.-O.; Cossi, M.; Schimmelpfennig, B.; Neogrady, P.; Seijo, L. *Comput. Mater. Sci.* **2003**, *28*, 222–239.

(76) Becke, A. D. *J. Chem. Phys.* **1993**, *98*, 5648–5652.

(77) Frisch, M. J.; Trucks, G. W.; Schlegel, H. B.; Scuseria, G. E.; Robb, M. A.; Cheeseman, J. R.; Montgomery, J. A., Jr.; Vreven, T.; Kudin, K. N.; Burant, J. C.; Millam, J. M.; Iyengar, S. S.; Tomasi, J.; Barone, V.; Mennucci, B.; Cossi, M.; Scalmani, G.; Rega, N.; Petersson, G. A.; Nakatsuji, H.; Hada, M.; Ehara, M.; Toyota, K.; Fukuda, R.; Hasegawa, J.; Ishida, M.; Nakajima, T.; Honda, Y.; Kitao, O.; Nakai, H.; Klene, M.; Li, X.; Knox, J. E.; Hratchian, H. P.; Cross, J. B.; Bakken, V.; Adamo, C.; Jaramillo, J.; Gomperts, R.; Stratmann, R. E.; Yazyev, O.; Austin, A. J.; Cammi, R.; Pomelli, C.; Ochterski, J. W.; Ayala, P. Y.; Morokuma, K. ; Voth, G. A. ; Salvador, P. ; Dannenberg, J. J. ; Zakrzewski, V. G.; Dapprich, S.; Daniels, A. D.; Strain, M. C.; Farkas, O.; Malick, D. K.; Rabuck, A. D.; Raghavachari, K.; Foresman, J. B.; Ortiz, J. V.; Cui, Q.; Baboul, A. G.; Clifford, S.; Cioslowski, J.; Stefanov, B. B.; Liu, G.; Liashenko, A.; Piskorz, P.; Komaromi, I.; Martin, R. L.; Fox, D. J.; Keith, T.; Al-Laham, M. A.; Peng, C. Y.; Nanayakkara, A.; Challacombe, M.; Gill, P. M. W.; Johnson, B.; Chen, W.; Wong, M. W.; Gonzalez, C.; Pople, J. A. *Gaussian 03*, Revision D.01; Gaussian, Inc.: Wallingford, CT, 2004.

(78) Finley, J.; Malmqvist, P.-Å.; Roos, B. O.; Serrano-Andrés, L. *Chem. Phys. Lett.* **1998**, *288*, 299–306.

(79) Ghigo, G.; Roos, B. O.; Malmqvist, P.-Å. *Chem. Phys. Lett.* **2004**, *396*, 142–149.

(80) Roos, B. O.; Andersson, K. *Chem. Phys. Lett.* **1995**, *245*, 215–223.

(81) Aquilante, F.; Malmqvist, P.-Å.; Pedersen, T. B.; Ghosh, A.; Roos, B. O. *J. Chem. Theory Comput.* **2008**, *4*, 694–702.

(82) *Aces II*, a quantum chemical program package written by Stanton, J. F.; Gauss, J.; Watts, J. D.; Szalay, P. G.; Bartlett, R. J. with contribution from Auer, A. A.; Bernholdt, D. B.; Christiansen, O.; Harding, M. E.; Heckert, M.; Heun, O.; Huber, C.; Jonsson, D.; Juselius, J.; Lauderdale, W. J.; Metzroth, T.; Ruud, K. and the integral packages *MOLECULE* (Almlof, J.; Taylor, P. R.), *Props* (Taylor, P. R.), and *ABACUS* (Helgaker, T.; Jensen, H. A. A.; Jørgensen, P.; Olsen, J.). See also: Stanton, J. F.; Gauss, J.; Watts, J. D.; Lauderdale, W. J.; Bartlett, R. J. *Int. J. Quantum Chem. Symp.* **1992**, *26*, 879. as well as http://www.aces2.de for the current version.

(83) *CFOUR*, a quantum chemical program package written by Stanton, J. F.; Gauss, J.; Harding, M. E.; Szalay, P. G. with contributions from Auer, A. A.; Bartlett, R. J.; Benedikt, U.; Berger, C.; Bernholdt, D. E.; Christiansen, O.; Heckert, M.; Heun, O.; Huber, C.; Jonsson, D.; Juselius, J.; Klein, K.; Lauderdale, W. J.; Matthews, D.; Metzroth, T.; O'Neill, D. P.; Price, D. R.; Prochnow, E.; Ruud, K.; Schiffmann, F.; Stopkowicz, S.; Varner, M. E.; Vázquez, J.; Wang, F.; Watts, J. D. and. the integral packages *MOLECULE* (Almlf, J.; Taylor, P. R.), *PROPS* (Taylor, P. R.), *ABACUS* (Helgaker,

T.; Jensen, H. J.; Jørgensen, P.; Olsen, J.),and *ECP* routines by Mitin, A. V.; van Wlle, C. For the current version, see http://www.cfour.de.

(84) *CHAMP* is a quantum Monte Carlo program package written by Umrigar, C. J.; Filippi, C. and collaborators.

(85) Burkatzki, M.; Filippi, C.; Dolg, M. *J. Chem. Phys.* **2007**, *126*, 234105.

(86) Filippi, C.; Umrigar, C. J. *J. Chem. Phys.* **1996**, *105*, 213–226. As the Jastrow correlation factor, we use the exponential of the sum of three fifth-order polynomials of the electron−nuclear (e−n), the electron−electron (e−e), and the pure three-body mixed e−e and e−n distances. The Jastrow factor is adapted to deal with pseudo-atoms, and the scaling factor κ is set to 0.60 a.u.

(87) Schmidt, M. W.; Baldridge, K. K.; Boatz, J. A.; Elbert, S. T.; Gordon, M. S.; Jensen, J. H.; Koseki, S.; Matsunaga, N.; Nguyen, K. A.; Su, S.; Windus, T. L.; Dupuis, M., Jr. *J. Comput. Chem.* **1993**, *14*, 1347–1363.

(88) Casula, M. *Phys. Rev. B* **2006**, *74*, 161102.

(89) Thom, H.; Dunning, J. *J. Chem. Phys.* **1989**, *90*, 1007−1023.

(90) Widmark, P.-O.; Malmqvist, P.-Å.; Roos, B. O. *Theor. Chem. Acc.* **1990**, *77*, 291–306.

(91) We add one s and one p diffuse function on the carbon and the nitrogen using exponents from the aug-cc-pVDZ basis set, taken from EMSL Basis Set Library (http://bse.pnl.gov).

(92) Nielsen, I. B.; Lammich, L.; Andersen, L. H. *Phys. Rev. Lett.* **2006**, *96*, 018304.

(93) Forbes, M. W.; Jockusch, R. A. *J. Am. Chem. Soc.* **2009**, *131*, 17038–17039.

(94) De Vico, L.; Olivucci, M.; Lindh, R. *J. Chem. Theory Comput.* **2005**, *1*, 1029–1037.

CT900692Y